FINAL TECHNICAL REPORT
AWARD NUMBER: G14AP00010

# Testing the EGF Method of Ground Motion Simulation using the Christchurch Earthquake Sequence


**Principal Investigator(s):**

Paul Somerville[1], Andreas Skarlatoudis & Jeff Bayless

AECOM
One California Plaza
300 S. Grand Avenue
Los Angeles, CA 90071


January 2014 - June 13, 2016




1. T: 213-996-2200;

   Email: paul.somerville@aecom.com

## TABLE OF CONTENTS

# Abstract

At distances within 10km of the source, the **M**6.1 Christchurch earthquake of 22 February 2011 generated ground motions that greatly exceeded the median predictions of ground motion prediction equations (GMPE's), and greatly exceeded the seismic design levels in the New Zealand Building Code (NZ1170.5:2004). This earthquake resulted in the almost complete destruction of the Christchurch Central Business District (CBD) – as many as 70% of the buildings in the CBD have been demolished as a result of this earthquake. In terms of damage ratio, this earthquake is the most devastating event to have ever occurred in a city having modern building codes like those in the United States.

The objective of this project is to test the Empirical Green's Function (EGF) method (Hartzell,1978; Irikura, 1986 and subsequent papers) for simulating the ground motions of large earthquakes in regions that have complex fault geometry and geological structure. We have evidence that the extremely damaging strong ground motions of the Canterbury earthquake sequence were influenced by a complex combination of rupture directivity and basin effects, in addition to soil amplification effects, which the EGF method may be able to reproduce.

We used recordings of the aftershocks as empirical Green's functions to simulate the recorded ground motions of the largest events in the earthquake sequence, including **M**6.2, 6.0 and 5.9 events. For rock site recordings, for which nonlinear effects are negligible, we directly use the EGF method. The EGF method is not directly applicable to the modeling of nonlinear soil effects because it is based on the linear superposition of the EGF's. However, the soil site recordings are of most interest because they represent the extremely damaging ground motions in the CBD. We overcome this problem by deconvolving EGFs to a reference stiff soil condition representing the gravels that underlie the soils and use these to simulate ground motion time series for the reference stiff soil condition. We validate the EGF approach in the time and frequency (response spectral) domains by comparison with observed strong-motion records and response spectra of the largest events of the sequence. Additionally, we assess the method's performance against ground motion simulations computed from a 3D hybrid simulation method.

# Introduction

The main events of the Canterbury earthquake sequence are summarized in Figure 1.

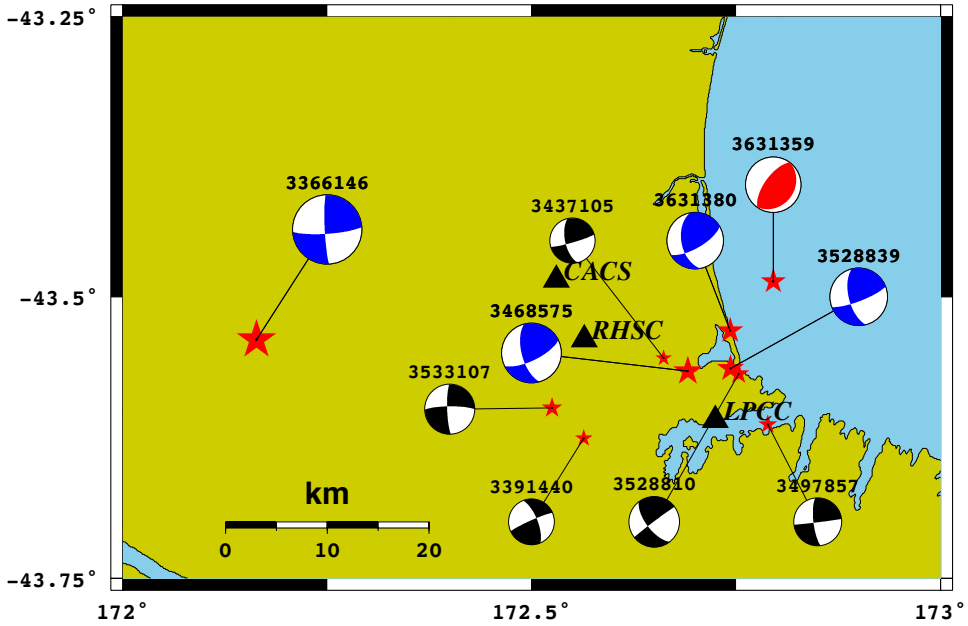


**Event Legend**

| ID | Date | Time | Mw | Depth | Dist2LPCC | Azimuth2LPCC | Dist2CACS | Azimuth2CACS | Length | Width | Rise Time |
|---|---|---|---|---|---|---|---|---|---|---|---|
| 3366146 | 2010-09-03 | 16:35:41.836 | 7.2 | 11.0 | 47.2 | 279.7 | 30.1 | 258.5 | 65.7 | 24.7 | 1.36 |
| 3391440 | 2010-10-18 | 22:32:15.901 | 4.8 | 5.0 | 14.1 | 262.1 | 16.0 | 170.2 | 2.4 | 2.7 | 0.09 |
| 3437105 | 2010-12-25 | 21:30:15.903 | 4.7 | 5.0 | 9.4 | 320.3 | 13.2 | 126.2 | 2.1 | 2.5 | 0.08 |
| 3468575 | 2011-02-21 | 23:51:42.320 | 6.2 | 5.4 | 7.9 | 330.6 | 15.9 | 124.9 | 16.5 | 9.8 | 0.47 |
| 3497857 | 2011-04-16 | 05:49:22.715 | 5.0 | 8.9 | 9.9 | 94.8 | 25.3 | 124.6 | 3.1 | 3.3 | 0.11 |
| 3528810 | 2011-06-13 | 01:01:00.348 | 5.3 | 8.9 | 9.9 | 26.6 | 20.2 | 117.4 | 4.8 | 4.3 | 0.16 |
| 3528839 | 2011-06-13 | 02:20:49.260 | 6.0 | 6.9 | 8.8 | 16.3 | 19.4 | 117.2 | 12.5 | 8.2 | 0.35 |
| 3533107 | 2011-06-21 | 10:34:22.999 | 5.2 | 8.8 | 18.3 | 274.2 | 12.8 | 181.8 | 4.1 | 3.9 | 0.14 |
| 3631359 | 2011-12-23 | 00:58:38.147 | 5.8 | 10.0 | 17.8 | 22.7 | 21.3 | 90.5 | 7.9 | 7.9 | 0.29 |
| 3631380 | 2011-12-23 | 02:18:03.590 | 5.9 | 7.5 | 9.0 | 9.4 | 18.0 | 106.4 | 10.9 | 7.5 | 0.31 |

**Figure 1.** Locations and focal mechanisms of the major events in the 2010 – 2012 Canterbury Earthquake Sequence. Stars indicate the locations of events, while triangles the locations of the sites at which we apply the EGF method. Beach-ball colors are used to denote the different source of the focal mechanism solutions (blue – Beavan et al., 2012; red – USGS; black - Geonet). Additional information on the events and source-site geometry are given in the figure legend.

Existing rupture models of the earthquake sequence are based mainly on the inversion of geodetic data (Holden and Beavan, 2012; Beavan et al, 2012), as shown in Figure 2. Except for the strike-slip, surface-faulting segment of the Darfield earthquake, shown by the red lines in Figure 3, the ruptures were all buried. The earthquake sequence involved rupture of a complex network of east-west striking strike-slip faults and northeast and northwest striking reverse faults whose inferred orientations are shown in Figure 3.

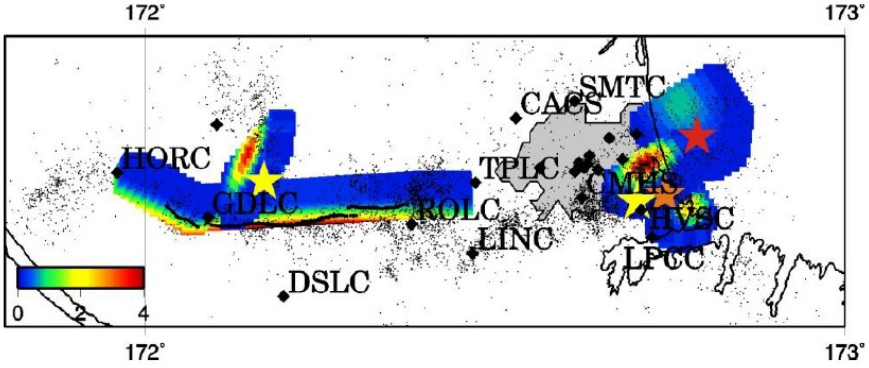


**Figure 2.** Slip distribution for the 2010-2011 Canterbury earthquake sequence. The yellow star to the left is the Darfield epicenter, the yellow star to the right and the orange and red stars are epicenters for the February, June and December earthquakes respectively. Black diamonds are strong motion stations. Source: Holden and Beavan (2012).

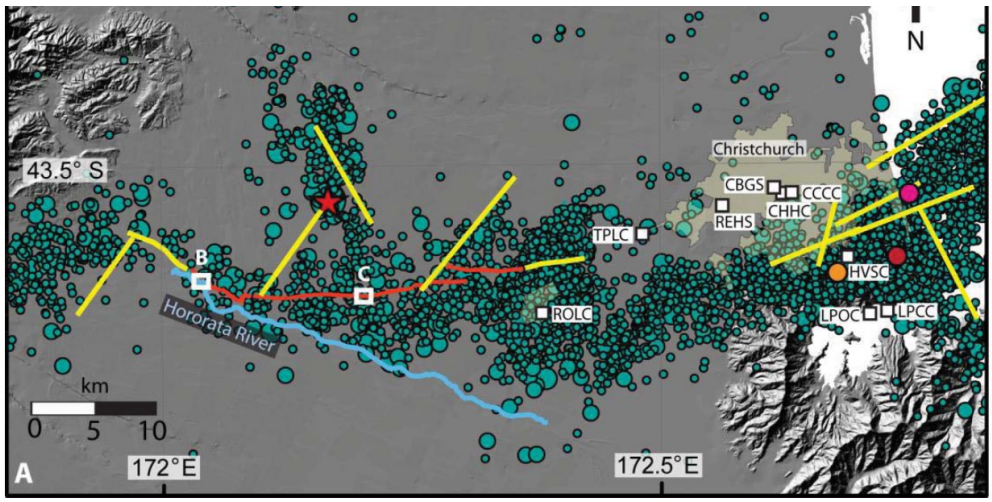


**Figure 3**. Epicenter locations for $M_L \geq 3.0$ events from Sept 4th 2010 to Feb 10th 2013 (www.geonet.org.nz), projected surface locations of major faults in yellow (from Beavan et al., 2011), location of mapped surface ruptures in red (from Quigley et al., 2012), and locations of selected strong ground motion stations. Source: Bradley et al. (2012).

Following the mainshock, a seismic refraction survey (Figure 4 left panel) identified the curved interface between the volcanic rock of the Lyttelton volcano and the overlying gravels and estuarine sediments (Figure 4 right panel). This basin structure gave rise to the strong basin waves that are evident in the mainshock strong motion recording at TPLC (Figure 5 left panel). These basin waves are absent from the strong motion recording ROLC (Figure 5 right panel), which is located outside the basin, but both recordings show strong fault-normal rupture directivity pulses that indicate forward rupture directivity.

The combination of forward rupture directivity effects and basin response appear to explain the destructive character of the strong ground motions, shown in Figure 6 for the

mainshock (left) and February aftershock (right). These effects are manifested in the peak in the response spectrum in the period range of 2 to 3.5 seconds, which greatly exceeded the New Zealand building code spectrum (NZ1170.5;2004).

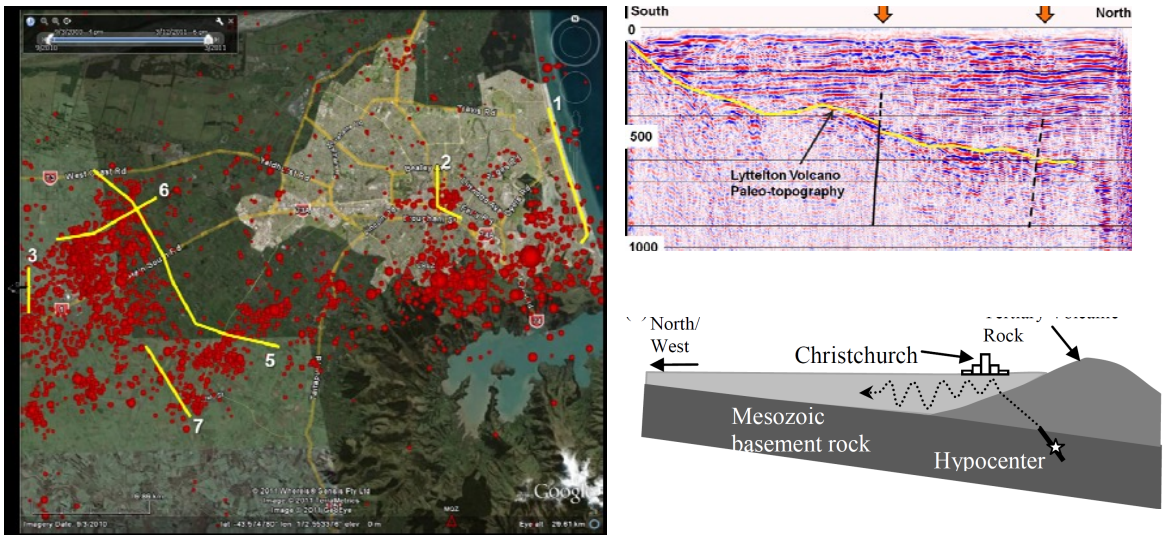


**Figure 4**. Left: locations of seismic reflection profiles, and Right top: Interpreted profile along Line 1 showing the location of the Port Hills fault on which the hypocenter of the February 2011 Mw 6.2 event is located. Source: Lawton et al., 2012. Right bottom: Schematic cross section of the Christchurch Basin. Source: Bradley and Cubrinovski (2011).

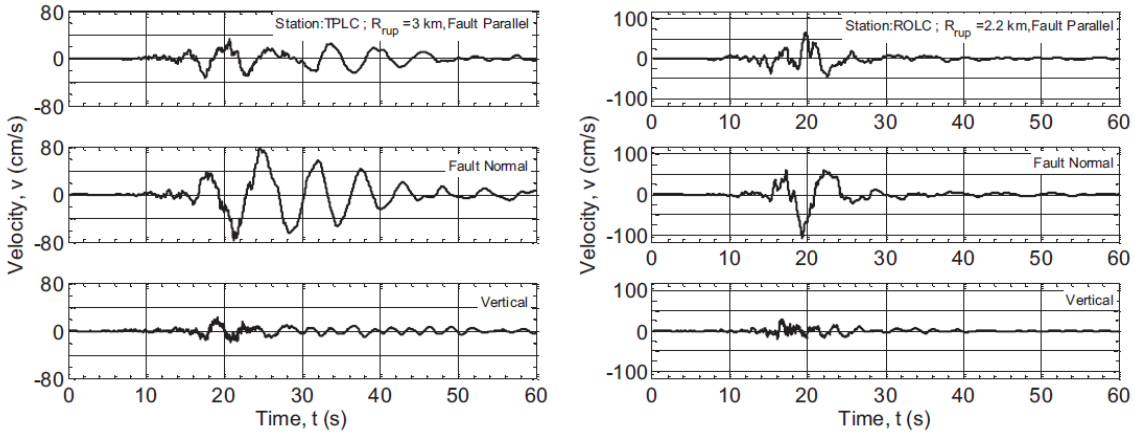


**Figure 5**. Large fault normal motions indicating strong forward directivity effects at locations to the east of the Greendale fault: (a) Templeton (TPLC), and (b) Rolleston (ROLC). The TPLC recording also contains basin effects. Source: Bradley et al. (2012).

The response spectra of the February earthquake exceeded the code spectrum over a wide band of periods. The strong nonlinear effects in soils are evident in the left side of Figure 7, which compares the soil and rock site recordings at Lyttelton. The soil evidently

amplified the ground motion at periods longer than 1 second, but strongly deamplified them at periods shorter than 0.5 seconds.

Because of the presence of rupture directivity and basin effects, empirical ground motion prediction equations do not provide a very reliable prediction of the recorded ground motion levels at periods of 1 and 3 seconds, as shown in Figure 8. All of the exceedances of the 84$^{th}$ percentile prediction lie within a closest distance of 10 km. If the large ground motions were explainable by an isotropic source effect such as high stress drop, we would expect the ground motions to be high at all distances, but this is not the case. This suggests that the large exceedances of the GMPE predictions were due to local conditions, including rupture directivity, basin effects and soil amplification effects.

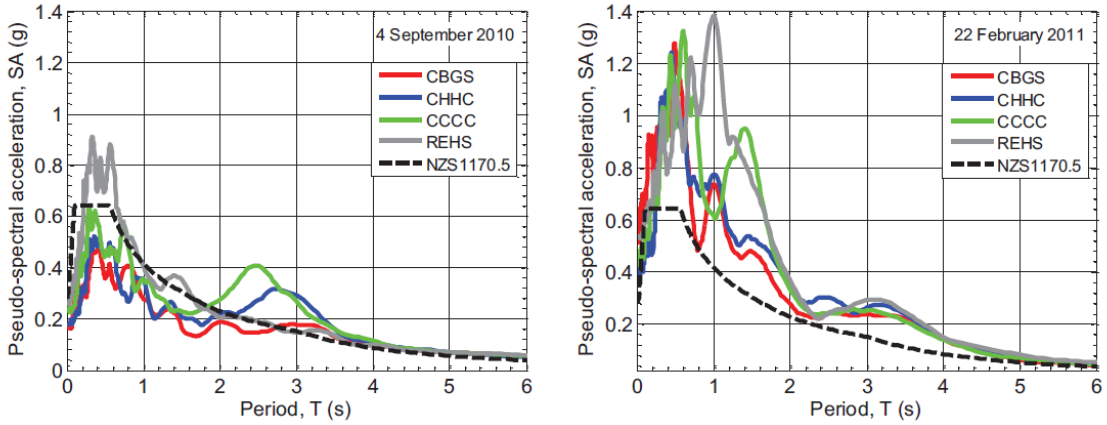


**Figure 6**. Geometric mean pseudo-spectral acceleration observed in the Christchurch CBD during the 4 September 2010 Darfield and 22 February 2011 Christchurch earthquakes. Source: Bradley et al., 2012.

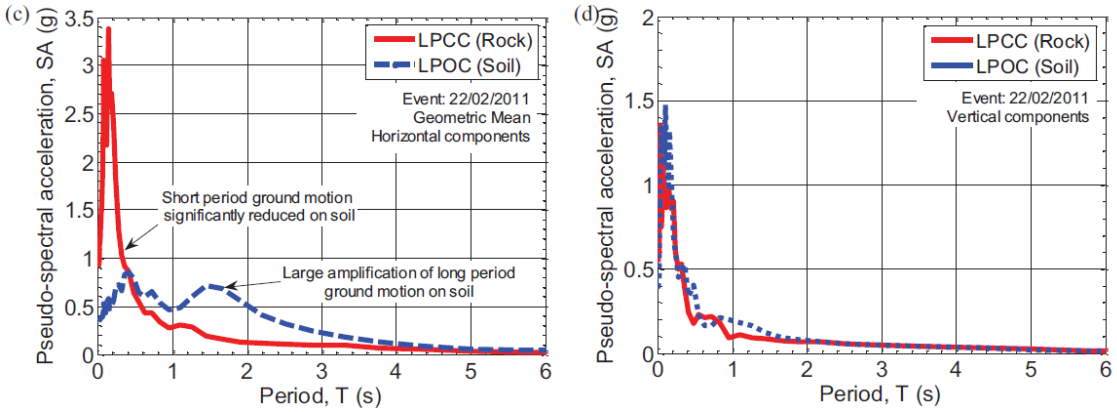


**Figure 7.** Comparison of the horizontal (left) and vertical (right) response spectra recorded on rock (LPCC) and soil (LPOC) at Lyttelton Port during the 22 February 2011 earthquake. Source: Bradley et al., 2012.

The surface geology of Christchurch is comprised of the Springston formation: fluvial gravels, sands and silts up to 20 m in thickness; and the Christchurch formation: estuarine, lagoon, dune, and coastal swamp deposits of gravel, sand, silt, clay and peat up to 40 m thick. The nature of this depositional environment causes significant variations in the characteristics of the shallow soil over small distances. These near surface sediments overlie 300- to 400-m of late Pleistocene sands and gravels, which in turn overly volcanic rock (Brown and Weeber, 1992).

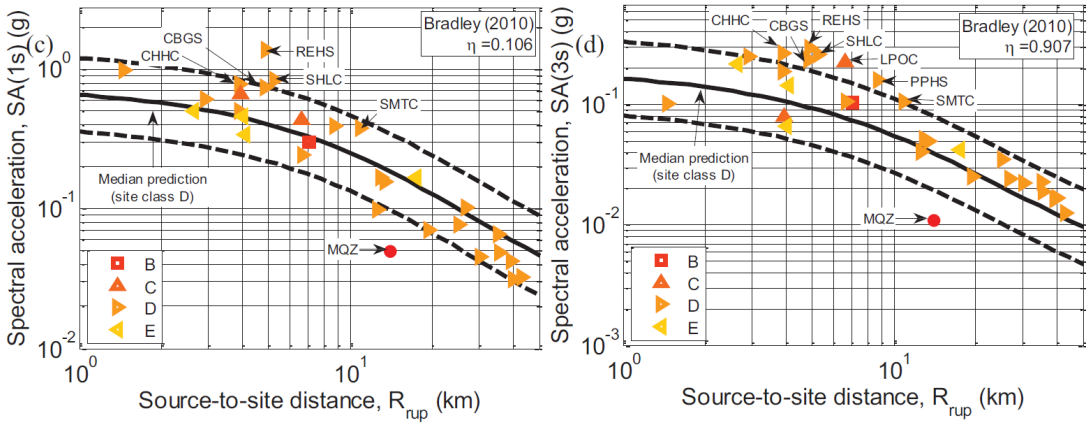


**Figure 8**. Comparison of pseudo-acceleration response spectral amplitudes observed in the 22 February 2011 Christchurch earthquake with empirical prediction equations (site class D soil conditions) for response spectral acceleration of 1 second (left) and 3 seconds (right). The median prediction by Bradley (2010) is given by the solid line and 16$^{th}$ and 84$^{th}$ percentiles by dashed lines. Source: Bradley and Cubrinovski (2011).

In Christchurch we have an opportunity to use the empirical Green's functions (recordings of small earthquakes; EGF) method, which uses aftershocks recorded at a station to simulate the ground motions recorded in larger earthquakes at that station. The EGF method originally proposed by Irikura (1986) was based on the summation of subevent records to maintain self-similar (uniform stress drop) omega squared source spectrum scaling between a subevent of a single size and the mainshock that is simulated; it could also allow for differences in stress drop between the subevent and mainshock. The summation of EGF's using kinematic modeling of the mainshock is coherent for longer periods (~N$^3$) and incoherently for high-frequencies (~N), where N is the number of subevents used, ensuring correct scaling at low and high frequencies, but leads to a deficiency in spectral amplitudes at intermediate frequencies (between the corner frequencies of the mainshock and the subevent. To correct this problem, Irikura and Kamae (1994) introduced a self-similar distribution of subevent fault sizes that removes the deficiency in amplitudes at intermediate frequencies. A schematic illustration of the EGF method is shown in Figure 9.

The mainshock time histories are produced by scaling the EGF-event records for distance using a scaling factor, and for rise-time differences between the subevent and mainshock

using a boxcar filter. The frequency range over which the simulations are reliable depends on the signal-to-noise ratio of the recordings of the EGF-events, which is controlled by the noise characteristics and the low-cut filter used in correcting the recordings.

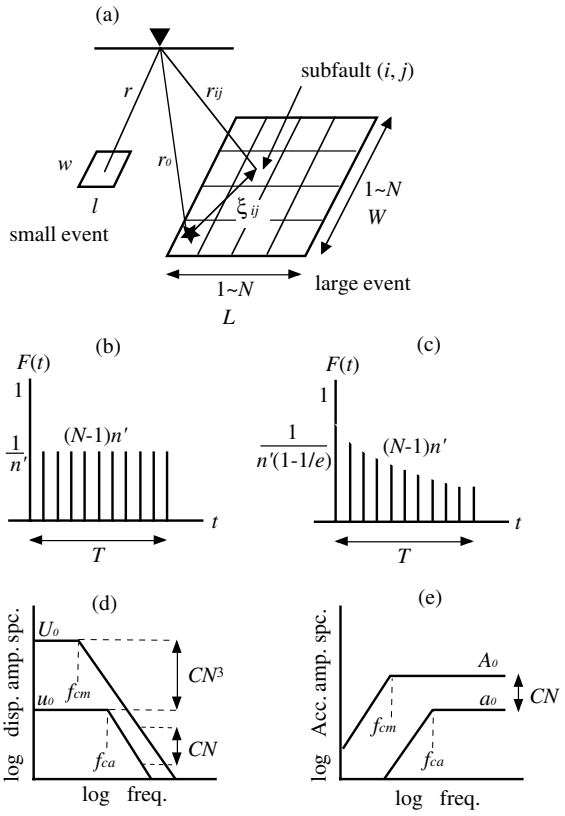


**Figure 9.** Schematic illustrations of the empirical Green's function method. (a) Fault areas of large and subenvents are defined to be $L$ X $W$ and $l$ X $w$, respectively, where $L/l=W/w=N$. (b) Filtering function $F(t)$ (after Irikura, 1986) to adjust to the difference in slip velocity function between the large and subenvents. This function is expressed as the sum of a delta and a boxcar function. (c) Modified filtering function (after Irikura *et al.*, 1997) with an exponentially decaying function instead of a boxcar function. $T$ is the rise time for the large event. (d) Schematic displacement amplitude spectra following the omega-squared source scaling model, assuming a stress drop ratio $C$ between the large and subenvents. (e) Acceleration amplitude spectra following the omega-squared source scaling model. Source: Miyake et al. (2003).

There are several reasons for preferring an EGF approach in Christchurch. It has the advantage of not requiring knowledge of the 3D structure or the calculation of Green's functions for that structure. This is an important advantage in Christchurch, because the subsurface geology of Christchurch is so complex that the accurate calculation of Green's functions may prove difficult. Second, abundant strong motion recordings of aftershocks of the Canterbury earthquake sequence are available for this purpose. Third, the EGF method can be applied for modeling directivity (e.g. Kamae and Irikura, 1998; Miyake et

al., 2006) and basin effects (Kamae et al., 1998), both of which have been shown to be important for the Christchurch earthquake sequence. We used the EGF method to simulate the strong motion recordings in Christchurch for the largest events of the aftershock sequence. At rock site recordings, for which nonlinear effects are negligible, the EGF method can be directly applied to simulate the recorded ground motions.

The soil site recordings are of most interest because they represent the extremely damaging ground motions in the CBD. However, in its standard form, the EGF method is not directly applicable to the modeling of nonlinear soil effects because it is based on the linear superposition of the EGFs. At short periods, standard EGF simulations will not account for the reduction of the ground motion amplitudes due to nonlinear soil behavior.

In order to account for the nonlinear soil behavior we used as EGFs ground motion recordings deconvolved to a reference stiff soil condition representing the gravels that underlie the alluvial deposits. These adjusted EGF's were used to simulate ground motion time series for the reference stiff soil condition. The deconvolved recordings used in this study come from the work of Markham et al. (2014) who performed a one-dimensional (1D) seismic site response analyses to represent the seismic response of potentially liquefiable soils during strong shaking.

# Application of the EGF method in the Christchurch sequence

We applied the EGF method to three events from the Christchurch sequence (see Figure 1) whose source parameters are shown in Table 1. We represented the source models of these three events by using records of subenvents as empirical Green's functions (subevents) whose focal mechanisms and hypocentral distances are similar to those of the large aftershock events that we model. We tested three subevents in order to assess the sensitivity of the method to the different EGF's. The source parameters of these events are also shown in Table 1 and their hypocentral locations in the map of Figure 1. The Lyttelton Port strong motion station (LPCC) has a $V_{S30}$ of about 792 m/s (Wood et al., 2011) and can be considered as a bedrock site. In the absence of any other strong motion stations on outcropping bedrock we selected ground motion recordings only from this station to use as EGF's.

**Table 1.** Seismological information of the large and subenvents used in the EGF method.

| Event ID | Latitude | Longitude | Depth | M | Strike° | Dip° | Rake° | Source |
|---|---|---|---|---|---|---|---|---|
| 3468575 | -43.5660 | 172.6909 | 5.4 | 6.2 | 64 | 70 | 151 | Bea12 |
| 3528839 | -43.5638 | 172.7431 | 6.9 | 6.0 | 69 | 78 | 151 | Bea12 |
| 3631380 | -43.5300 | 172.7428 | 7.5 | 5.9 | 60 | 69 | 136 | Bea12 |
| 3391440 | -43.6256 | 172.5636 | 5.0 | 4.8 | 246 | 84 | 6 | Geonet |
| 3437105 | -43.5544 | 172.6615 | 5.0 | 4.7 | 74 | 84 | 6 | Geonet |
| 3528810 | -43.5684 | 172.7531 | 8.9 | 5.3 | 233 | 88 | -2 | Geonet |

We used the EGFM (v1.2) computer code (Irikura, 1986; Irikura and Kamae, 1994) implementation of the EGF method. The parameters used by the code to describe the source (both element and target event) and site properties are listed in Table 2.

**Table 2.** Definitions of the parameters used in the EGFM code.

| PARAMETER | DEFINITION |
|---|---|
| **Strike (element & target)** | Fault strike (degree) |
| **Dip (element & target)** | Fault dip (degree) |
| **Rake (element & target)** | Fault Rake (degree) |
| **Depth (element & target)** | Hypocentral depth (km) |
| **dx** | Length of the fault along strike (km) |
| **dw** | Length of the fault along the dip direction (km) |
| **tra** | Rise time of the element event (s) |
| **nx** | Number of subfaults along the strike direction |
| **nw** | Number of subfaults in the downdip direction |
| **nt** | Number of the element events summed up at each subfault |
| **nsx** | Location of the rupture starting point along strike |
| **nsw** | Location of the rupture starting point In the downdip direction |
| **cfactor** | Parameter to correct the difference in stress drop between the element event and the mainshock |
| **Vs** | S-wave velocity of the medium (km/s) |
| **Vr** | Rupture velocity (km/s) |
| **ird** | Style of rupture propagation |
| **ipfm** | Radiation pattern correction |
| **Repi** | Epicentral distance (km) |
| **Az** | Azimuth (degree) |
| **Cmp** | Component orientation (degree) |
| **IMDL** | Shape of the slip time function |

We assumed an S-wave velocity ($V_s$) of 6.5 km/s along the wave propagation path and a rupture velocity of 5.2 km/sec ($0.8V_s$) on the fault plane. All simulations were performed in the 0.25-40 Hz frequency band to account for the signal-to-noise ratio of the element events. The average rise time on the fault is calculated using the following relationship from Somerville et al. (2001) in which $M_0$ is the seismic moment:

$$T_r = 1.6 \times 10^{-9} M_0^{\frac{1}{3}} \quad (1)$$

The fault dimensions for each event in Table 1 were estimated using the Leonard (2010) magnitude-rupture area and magnitude-fault length relationships developed for tectonically active regions. The results from applying the EGF method on the selected events are presented in the following sections.

## Simulation of 2011-02-21, 23:51:42, M6.2 Event at LPCC

The values of the parameters used in the simulation of the 2011-02-21, 23:51:42, **M**6.2 Event at LPCC are shown in Table 3. The comparison of the EGF results with the observed ground motions, using the 2010-10-18, 22:32:15, **M**4.8 as element event, is shown in Figures 10 and 11. Similarly the results using the 2010-12-25, 21:30:15, **M**4.7 as element event is shown in Figures 12 and 13. Finally the results using the 2011-06-13, 01:01:00, **M**5.3 as element event are shown in Figures 14 and 15.

**Table 3.** Parameter values used in the EGF method.

| | **2010-10-18 22:32:15** | | **2010-10-25 21:30:15** | | **2011-06-13 01:01:00** | |
|---|---|---|---|---|---|---|
| Parameter | ***x-component*** | ***y-component*** | ***x-component*** | ***y-component*** | ***x-component*** | ***y-component*** |
| dx | 2.1 | 2.1 | 2.2 | 2.2 | 4.8 | 4.8 |
| dw | 1.9 | 1.9 | 1.8 | 1.8 | 4.3 | 4.3 |
| tra | 0.09 | 0.09 | 0.06 | 0.06 | 0.16 | 0.16 |
| nx | 5 | 5 | 5 | 5 | 6 | 6 |
| nw | 5 | 5 | 5 | 5 | 6 | 6 |
| nt | 5 | 5 | 5 | 5 | 6 | 6 |
| ntt | 28 | 28 | 28 | 28 | 28 | 28 |
| nsx | 5 | 5 | 1 | 1 | 2 | 2 |
| nsw | 5 | 5 | 5 | 5 | 4 | 4 |
| cfactor | 3.4 | 3.4 | 5 | 5 | 1 | 1 |
| ird | 2 | 2 | 2 | 2 | 2 | 2 |
| ipfm | 0 | 0 | 0 | 0 | 0 | 0 |
| Cmp | 350 | 260 | 350 | 260 | 350 | 260 |
| imdl | 3 | 3 | 3 | 3 | 3 | 3 |

## *2010-10-18, 22:32:15, M4.8 element event*

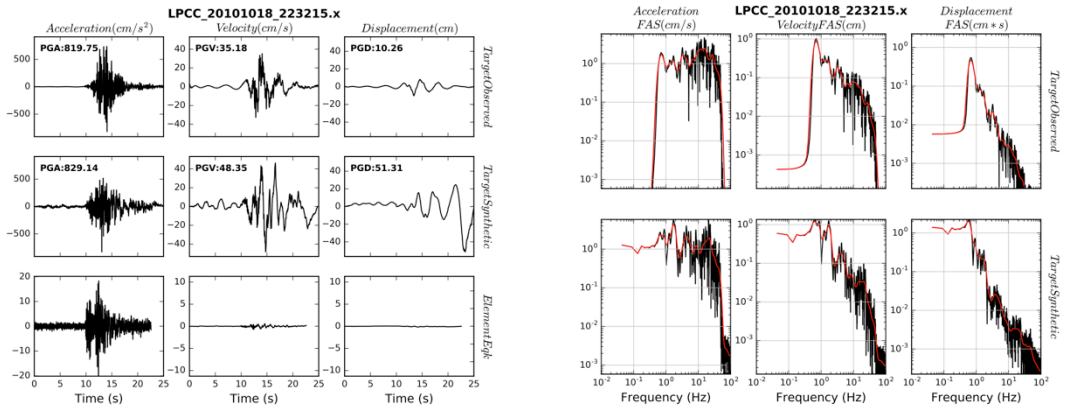


**Figure 10.** Comparison of simulations with data in the time (left) and frequency (right) domains for the x horizontal component, using as element event the 2010-10-18, 22:32:15, **M**4.8 earthquake. For both plots, the left hand side column corresponds to ground acceleration, the middle to ground velocity and the right to ground displacement. In the left figure the top row shows the data, the middle row the simulations and the bottom row the element event used in the simulations. In the right figure the black lines correspond to the FAS of data (top row) and simulations (bottom row), while the red lines show the smoothed FAS using Konno and Ohmachi (1998) smoothing. Colors and notations have been kept the same for this type of figure throughout the manuscript.

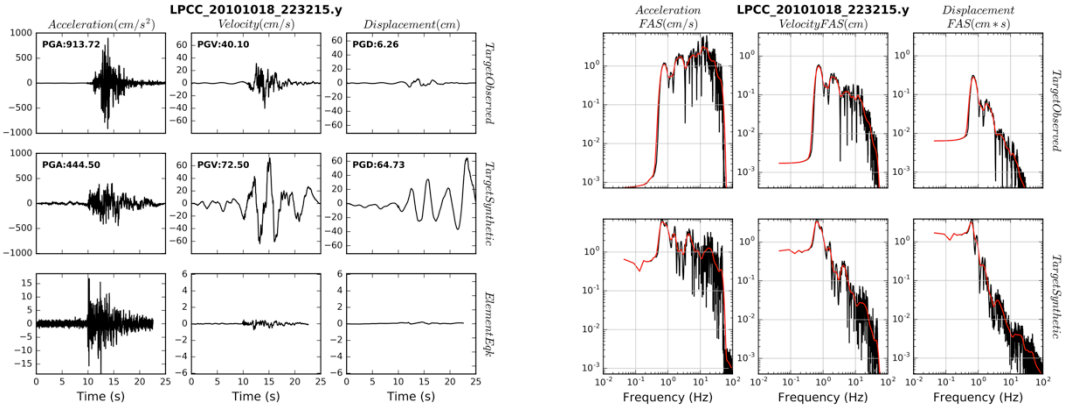


**Figure 11.** Comparison of simulations with data in the time and frequency domains for the y horizontal component, using as element event the 2010-10-18, 22:32:15, **M**4.8 earthquake.

## *2010-12-25, 21:30:15, M4.7 element event*

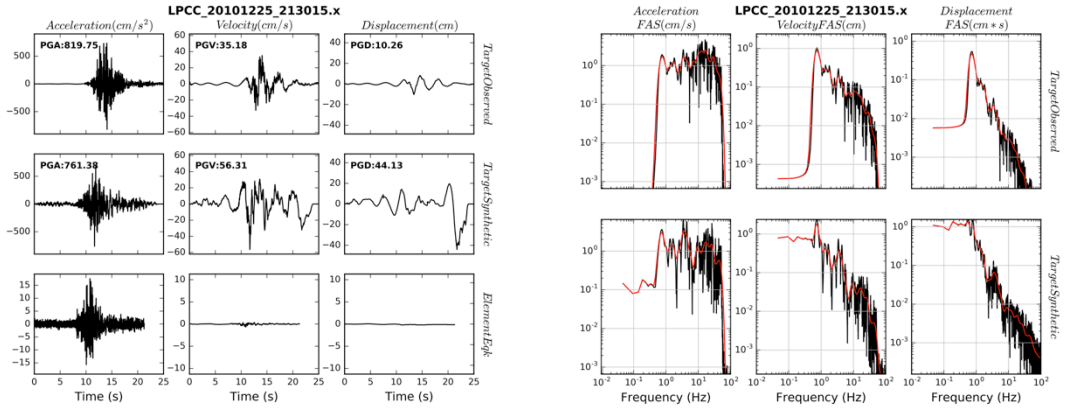


**Figure 12.** Comparison of simulations with data in the time and frequency domains for the x horizontal component, using as element event the 2010-12-25, 21:30:15, **M**4.7 earthquake.

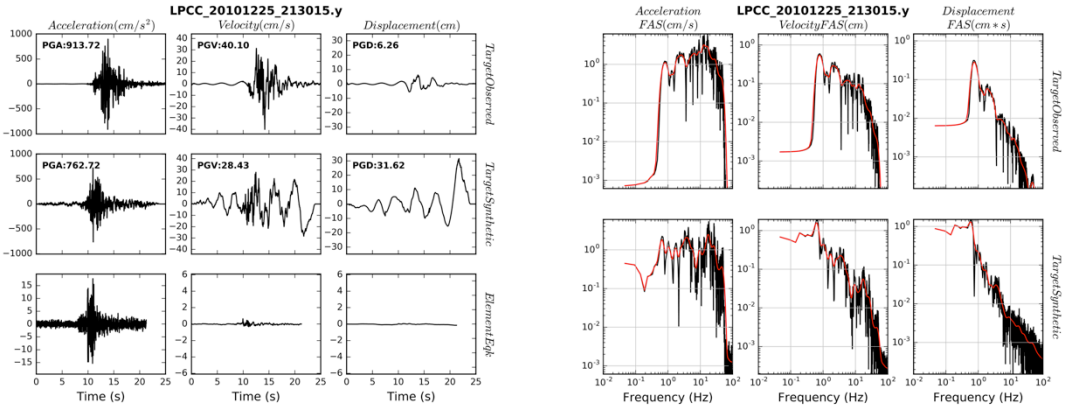


**Figure 13.** Comparison of simulations with data in the time and frequency domains for the y horizontal component, using as element event the 2010-12-25, 21:30:15, **M**4.7 earthquake.

## *2011-06-13, 01:01:00, M5.3 element event*

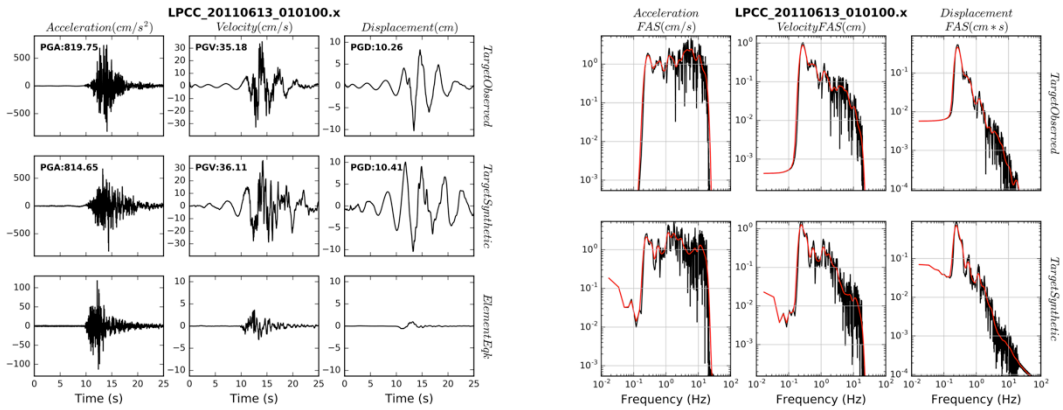


**Figure 14.** Comparison of simulations with data in the time and frequency domains for the x horizontal component, using as element event the 2011-06-13, 01:01:00, **M**5.3 earthquake.

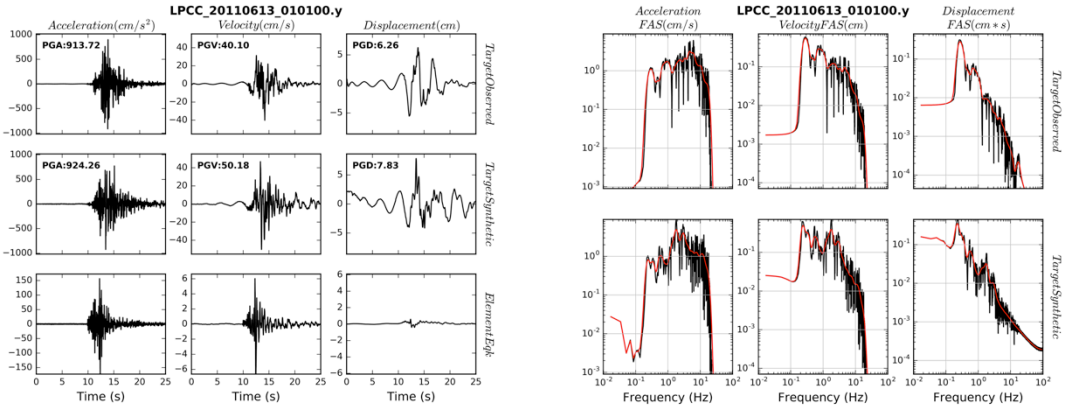


**Figure 15.** Comparison of simulations with data in the time and frequency domains for the y horizontal component, using as element event the 2011-06-13, 01:01:00, **M**5.3 earthquake.

# Simulation of 2011-06-13, 02:20:49, M6.0 Event at LPCC

The values of the parameters used in the simulation of the 2011-06-13, 02:20:49, **M**6.0 Event at LPCC are shown in Table 4. The comparison of the EGF results with the observed ground motions, using the 2010-10-18, 22:32:15, **M**4.8 as element event, is shown in Figures 16 and 17. Similarly the results using the 2010-12-25, 21:30:15, **M**4.7 as element event is shown in Figures 18 and 19. Finally the results using the 2011-06-13, 01:01:00, **M**5.3 as element event are shown in Figures 20 and 21.

**Table 4.** Parameter values used in the EGF method.

| | **2010-10-18 22:32:15** | | **2010-10-25 21:30:15** | | **2011-06-13 01:01:00** | |
|---|---|---|---|---|---|---|
| Parameter | ***x-component*** | ***y-component*** | ***x-component*** | ***y-component*** | ***x-component*** | ***y-component*** |
| dx | 2.1 | 2.1 | 2.2 | 2.2 | 4.8 | 4.8 |
| dw | 1.9 | 1.9 | 1.8 | 1.8 | 4.3 | 4.3 |
| tra | 0.09 | 0.09 | 0.06 | 0.06 | 0.16 | 0.16 |
| nx | 5 | 5 | 5 | 5 | 6 | 6 |
| nw | 5 | 5 | 5 | 5 | 6 | 6 |
| nt | 5 | 5 | 5 | 5 | 6 | 6 |
| ntt | 28 | 28 | 28 | 28 | 28 | 28 |
| nsx | 5 | 5 | 1 | 1 | 2 | 2 |
| nsw | 5 | 5 | 5 | 5 | 4 | 4 |
| cfactor | 3.4 | 3.4 | 5 | 5 | 1 | 1 |
| ird | 2 | 2 | 2 | 2 | 2 | 2 |
| ipfm | 0 | 0 | 0 | 0 | 0 | 0 |
| Cmp | 350 | 260 | 350 | 260 | 350 | 260 |
| imdl | 3 | 3 | 3 | 3 | 3 | 3 |

## *2010-10-18, 22:32:15, M4.8 element event*

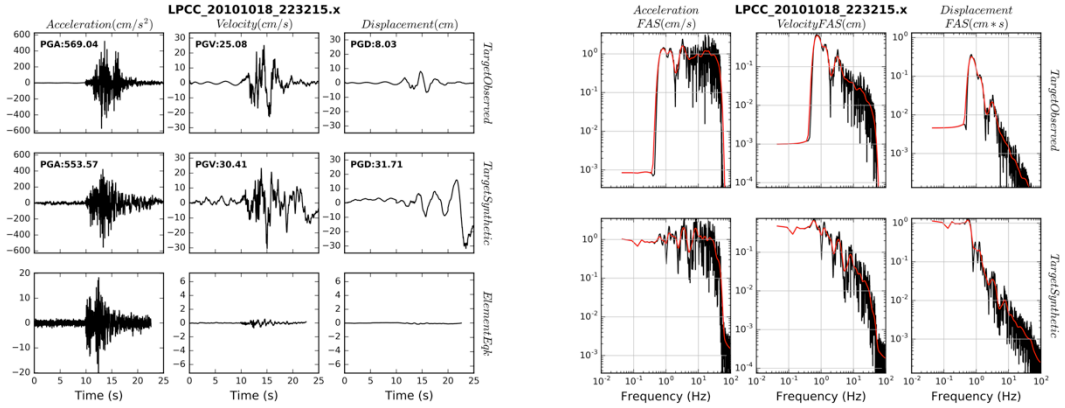


**Figure 16.** Comparison of simulations with data in the time and frequency domains and Arias intensity for the x horizontal component, using as element event the 2010-10-18, 22:32:15, **M**4.8 earthquake.

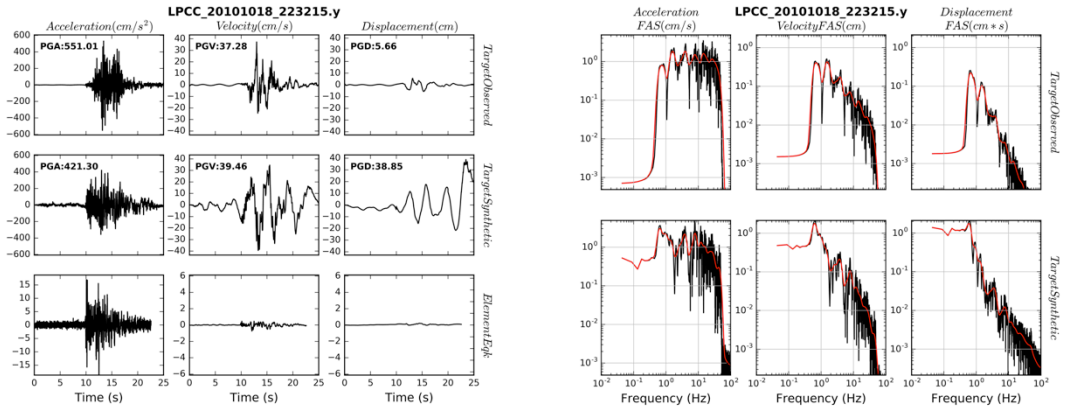


**Figure 17.** Comparison of simulations with data in the time and frequency domains for the y horizontal component, using as element event the 2010-10-18, 22:32:15, **M**4.8 earthquake.

## *2010-12-25, 21:30:15, M4.7 element event*

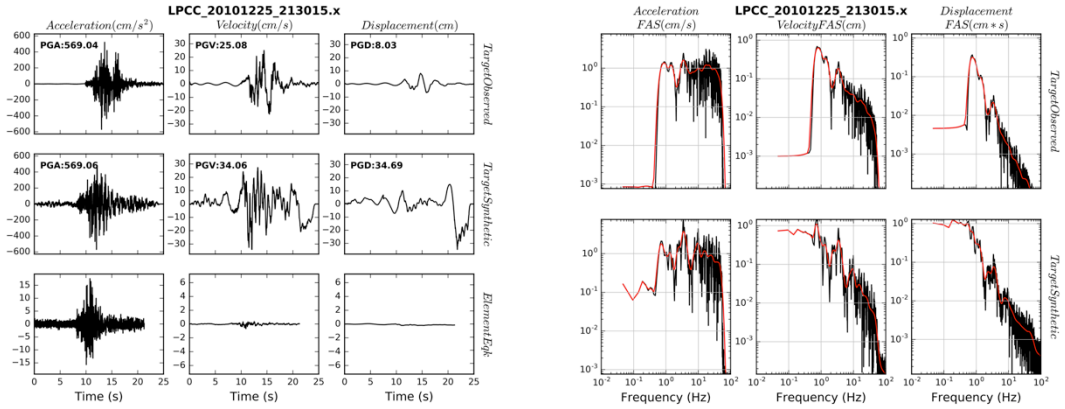


**Figure 18.** Comparison of simulations with data in the time and frequency domains for the x horizontal component, using as element event the 2010-12-25, 21:30:15, **M**4.7 earthquake.

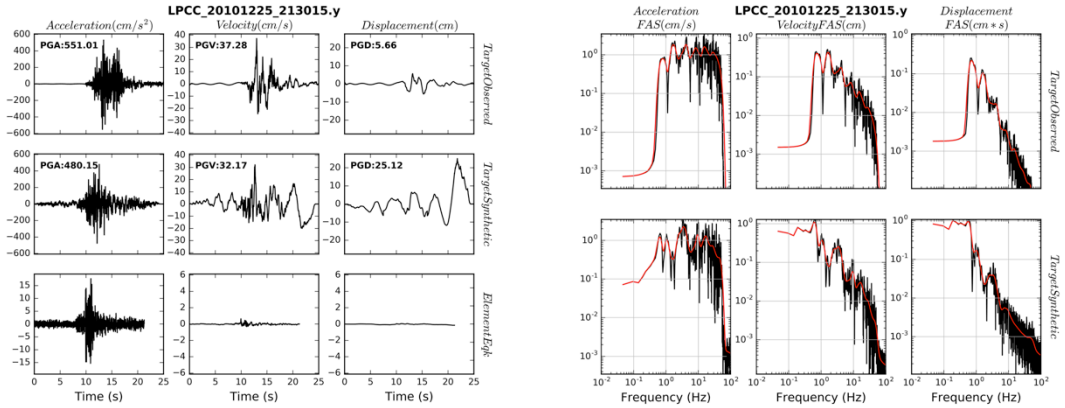


**Figure 19.** Comparison of simulations with data in the time and frequency domains for the x horizontal component, using as element event the 2010-12-25, 21:30:15, **M**4.7 earthquake.

## *2011-06-13, 01:01:00, M5.3 element event*

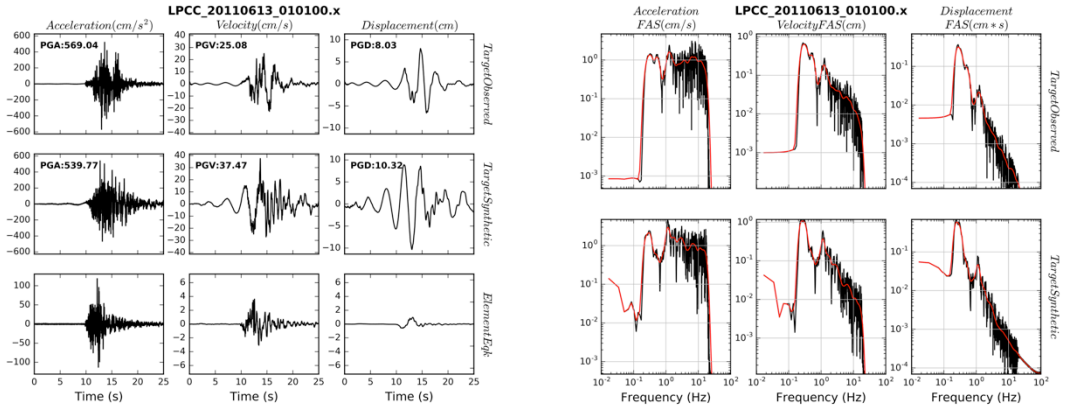


**Figure 20.** Comparison of simulations with data in the time and frequency domains for the x horizontal component, using as element event the 2011-06-13, 01:01:00, **M**5.3 earthquake.

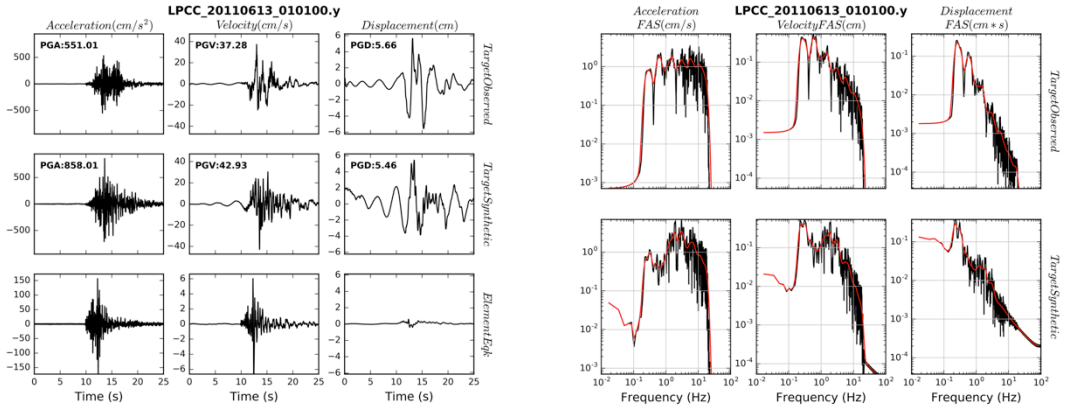


**Figure 21.** Comparison of simulations with data in the time and frequency domains for the y horizontal component, using as element event the 2011-06-13, 01:01:00, **M**5.3 earthquake.

## Simulation of 2011-12-23, 02:18:03, M5.9 Event at LPCC

The values of the parameters used in the simulation of the 2011-12-23, 02:18:03, **M**5.9 Event at LPCC are shown in Table 5. The comparison of the EGF results with the observed ground motions, using the 2010-10-18, 22:32:15, **M**4.8 as element event, is shown in Figures 22 and 23. Similarly the results using the 2010-12-25, 21:30:15, **M**4.7 as element event is shown in Figures 24 and 25. Finally the results using the 2011-06-13, 01:01:00, **M**5.3 as element event are shown in Figures 26 and 27.

**Table 5.** Parameter values used in the EGF method.

| | **2010-10-18 22:32:15** | | **2010-10-25 21:30:15** | | **2011-06-13 01:01:00** | |
|---|---|---|---|---|---|---|
| Parameter | ***x-component*** | ***y-component*** | ***x-component*** | ***y-component*** | ***x-component*** | ***y-component*** |
| dx | 2.1 | 2.1 | 2.2 | 2.2 | 4.8 | 4.8 |
| dw | 1.9 | 1.9 | 1.8 | 1.8 | 4.3 | 4.3 |
| tra | 0.09 | 0.09 | 0.06 | 0.06 | 0.16 | 0.16 |
| nx | 5 | 5 | 5 | 5 | 6 | 6 |
| nw | 5 | 5 | 5 | 5 | 6 | 6 |
| nt | 5 | 5 | 5 | 5 | 6 | 6 |
| ntt | 28 | 28 | 28 | 28 | 28 | 28 |
| nsx | 5 | 5 | 1 | 1 | 2 | 2 |
| nsw | 5 | 5 | 5 | 5 | 4 | 4 |
| cfactor | 3.4 | 3.4 | 5 | 5 | 1 | 1 |
| ird | 2 | 2 | 2 | 2 | 2 | 2 |
| ipfm | 0 | 0 | 0 | 0 | 0 | 0 |
| Cmp | 350 | 260 | 350 | 260 | 350 | 260 |
| imdl | 3 | 3 | 3 | 3 | 3 | 3 |

## *2010-10-18, 22:32:15, M4.8 element event*

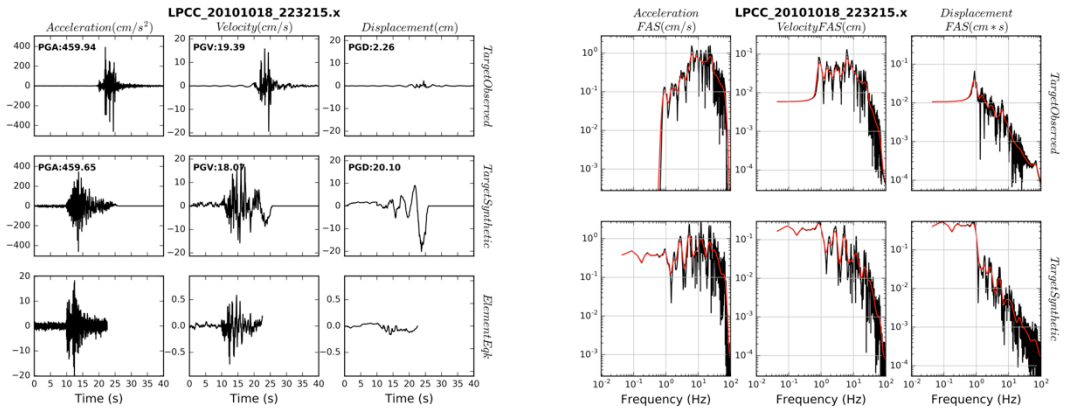


**Figure 22.** Comparison of simulations with data in the time and frequency domains for the x horizontal component, using as element event the 2010-10-18, 22:32:15, **M**4.8 earthquake.

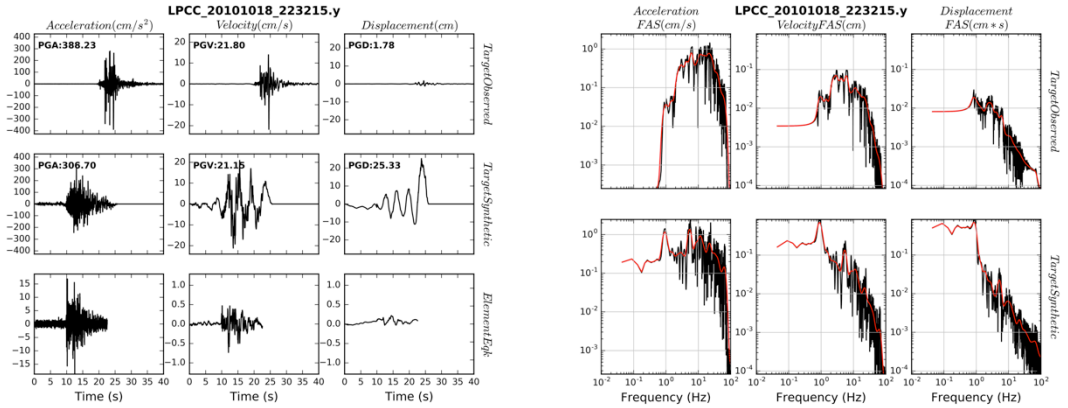


**Figure 23.** Comparison of simulations with data in the time and frequency domains for the x horizontal component, using as element event the 2010-10-18, 22:32:15, **M**4.8 earthquake.

## *2010-12-25, 21:30:15, M4.7 element event*

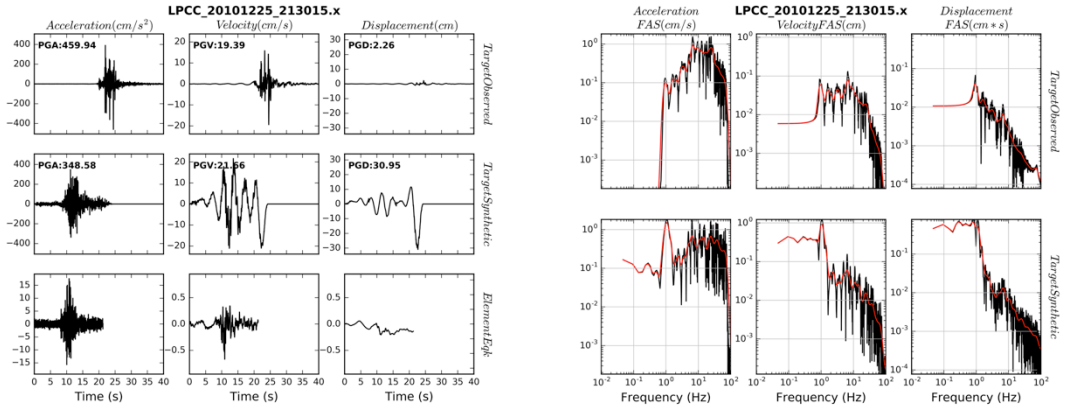


**Figure 24.** Comparison of simulations with data in the time and frequency domains for the x horizontal component, using as element event the 2010-12-25, 21:30:15, **M**4.7 earthquake.

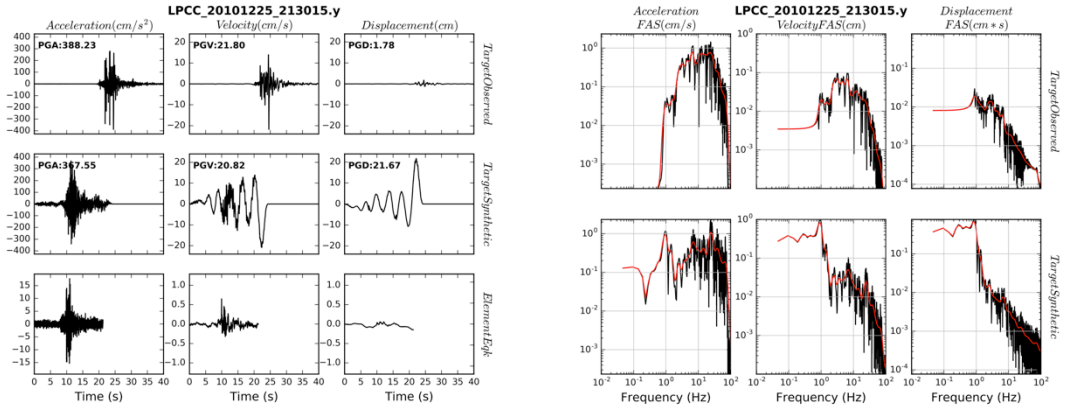


**Figure 25.** Comparison of simulations with data in the time and frequency domains for the y horizontal component, using as element event the 2010-12-25, 21:30:15, **M**4.7 earthquake.

## *2011-06-13, 01:01:00, M5.3 element event*

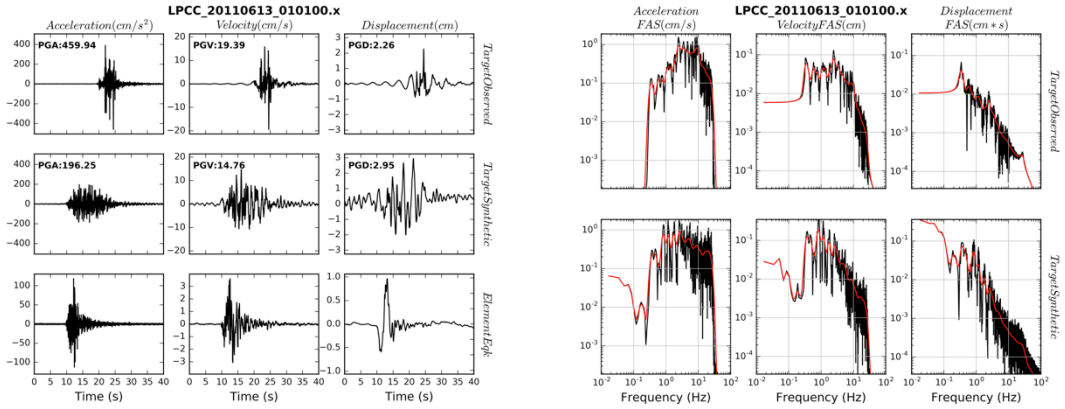


**Figure 26.** Comparison of simulations with data in the time and frequency domains for the x horizontal component, using as element event the 2011-06-13, 01:01:00, **M**5.3 earthquake.

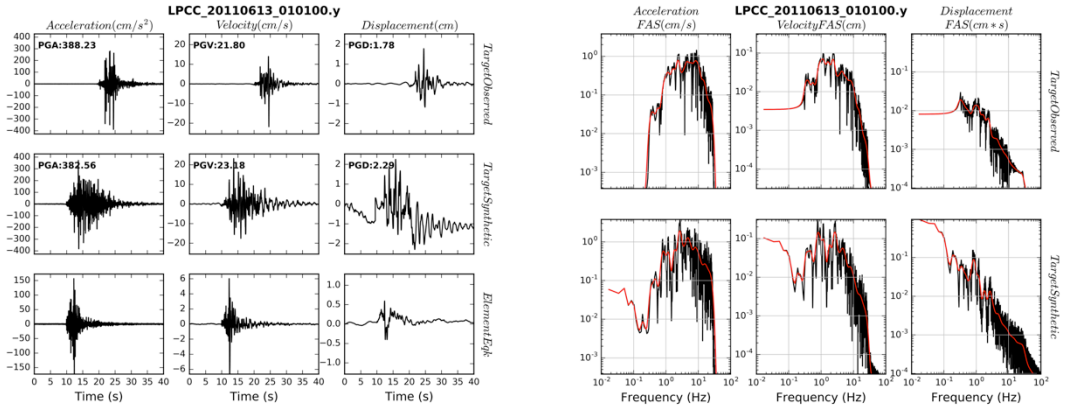


**Figure 27.** Comparison of simulations with data in the time and frequency domains for the y horizontal component, using as element event the 2011-06-13, 01:01:00, **M**5.3 earthquake.

## Deconvolved ground motions

In the previous sections we presented the results from the application of the EGF method to recordings at the LPCC strong motion station. However, soil site recordings are of most interest because they represent the extremely damaging ground motions in the CBD. As already mentioned, the EGF method in its standard form cannot be applied to simulate recordings at soil sites exhibiting non-linearity since it does not properly account for the presence of nonlinear soil effects as it is based on the linear superposition of EGF's.

In order to overcome this problem, we used as EGF's ground motion recordings deconvolved to a reference stiff soil condition representing the gravels that underlie the alluvial deposits. These adjusted EGF's were used to simulate ground motions for the reference stiff soil condition. The deconvolved recordings used in this study come from the work of Markham et al. (2014). They performed an equivalent linear analysis, which allows for the linear deconvolution of surface motions from any one point to another in a 1D soil column.

The deconvolution analysis in Markham et al. (2014) was performed with SHAKE2000 (Ordonez, 2000) and was based on the steps recommended in Silva (1988).

1. Low pass filter ($4^{th}$ order, Butterworth) recorded surface motion at 15Hz and scale by 0.87.
2. Input motion at surface using an equivalent linear analysis
3. Obtain motion from layer of interest at depth
4. Obtain the final iteration values of shear modulus reduction ($G/G_{max}$) and material damping ($\lambda$) for each layer during the deconvolution process
5. Using a linear analysis with the final values from step 4 for each layer, perform the deconvolution process again by placing the LP filtered, unscaled, surface motion at the surface and obtain the "final", outcropping, deconvolved motion.

A schematic overview of the described procedure is shown in Figure 28.

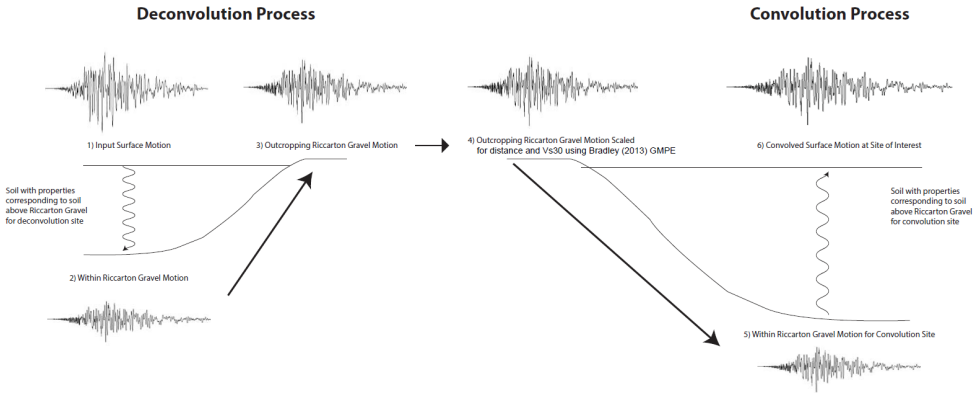


**Figure 28.** Overview of the deconvolution process. Source: Markham et al. (2014).

## Selected Strong Motion Station Sites (CACS and RHSC)

Markham et al. (2014) used the Canterbury Aero Club station (CACS) and the Riccarton High School station (RHSC) sites in the deconvolution procedure. The site locations are shown in Figure 1. They selected these sites because:

- They are located on soil that did not show surface manifestations of liquefaction during any of the events of interest
- They are believed to have shown minimal nonlinear response during shaking
- The depth to the Riccarton gravel layer for these sites is the lowest among the 13 strong motion station sites listed, which requires the surface motion to be deconvolved only over a relatively shallow profile.

Unfortunately, recordings for the subevents that we originally selected to use in our analysis were not available at RHSC site, so we only present results for the CACS site.

The $V_s$ profiles used in the deconvolution at the CACS site are shown in Figure 29. Two depths for the Riccarton gravel depth were considered to account for the epistemic uncertainty in the site characterization of this station.

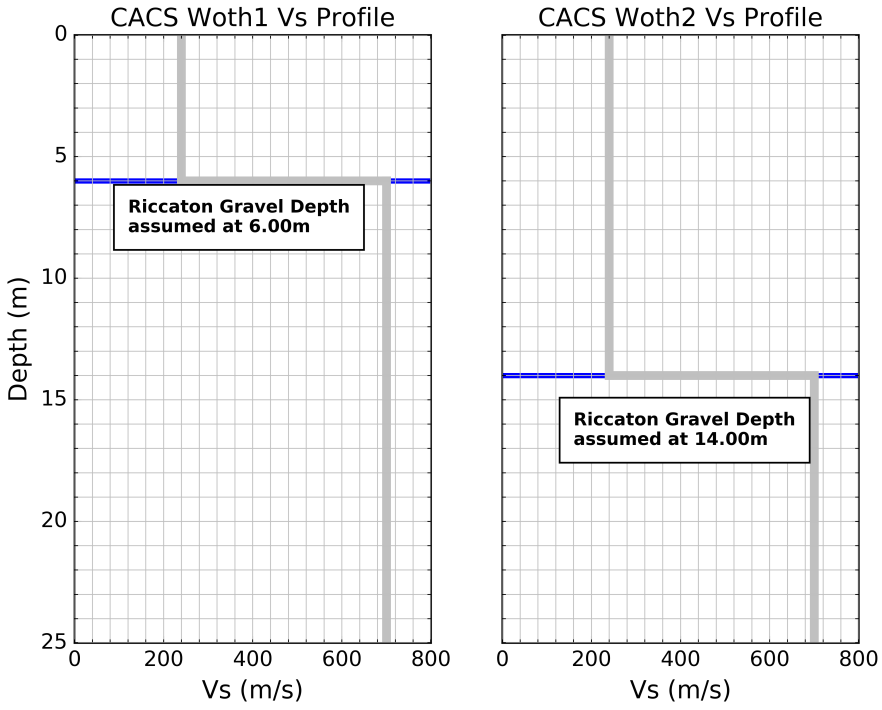


**Figure 29.** Shear wave velocity profiles for CACS strong motion station.

## Simulation of 2011-02-21, 23:51:42, M6.2 Event at CACS – Deconvolved

The values of the parameters used in the simulation of the 2011-02-21, 23:51:42, **M**6.2 Event at CACS are shown in Table 6. The comparison of the EGF results with the observed ground motions, using the 2010-12-25, 21:30:15, **M**4.7 as element event is shown in Figures 30 and 31 for the Woth1 $V_s$ profile and in Figures 32 and 33 for the Woth2 $V_s$ profile.

**Table 6.** Parameter values used in the EGF method.

| | **2010-10-25 21:30:15** | |
|---|---|---|
| Parameter | ***FN-component*** | ***FP-component*** |
| dx | 2.2 | 2.2 |
| dw | 1.8 | 1.8 |
| tra | 0.1 | 0.1 |
| nx | 5 | 5 |
| nw | 5 | 5 |
| nt | 5 | 5 |
| ntt | 28 | 28 |
| nsx | 1 | 1 |
| nsw | 5 | 5 |
| cfactor | 1.5 | 1.5 |
| ird | 2 | 2 |
| ipfm | 0 | 0 |
| Cmp | 90 | 0 |
| imdl | 3 | 3 |

## *2010-12-25, 21:30:15, M4.7 element event*

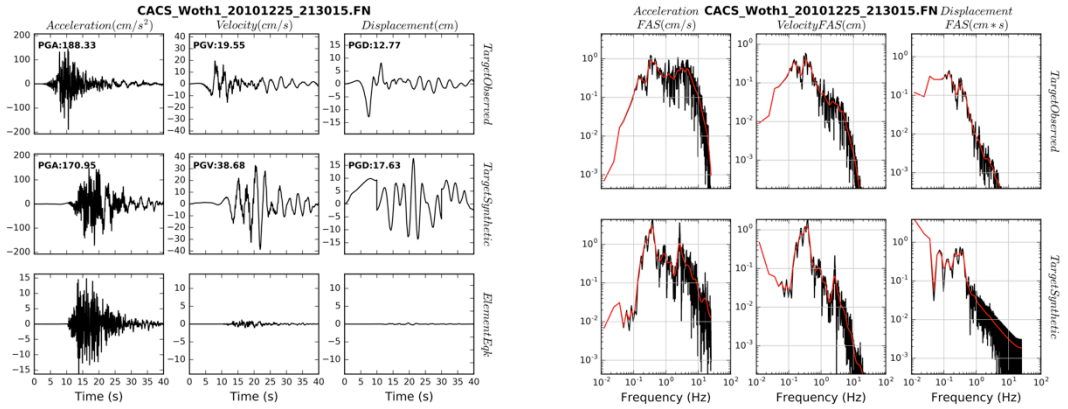


**Figure 30.** Comparison of simulations with data in the time and frequency domains for the fault-normal component, using as element event the 2010-12-25, 21:30:15, **M**4.7 earthquake for the Woth1 velocity profile.

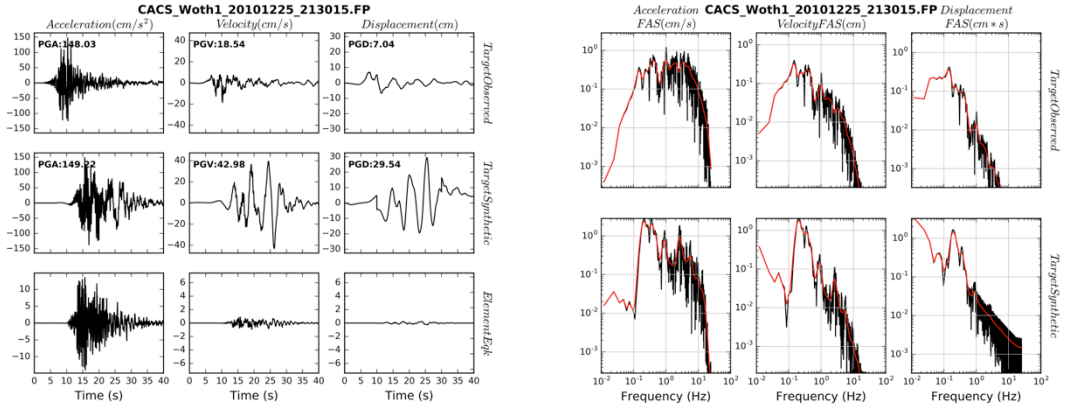


**Figure 31.** Comparison of simulations with data in the time and frequency domains for the fault-parallel component, using as element event the 2010-12-25, 21:30:15, **M**4.7 earthquake for the Woth1 velocity profile.

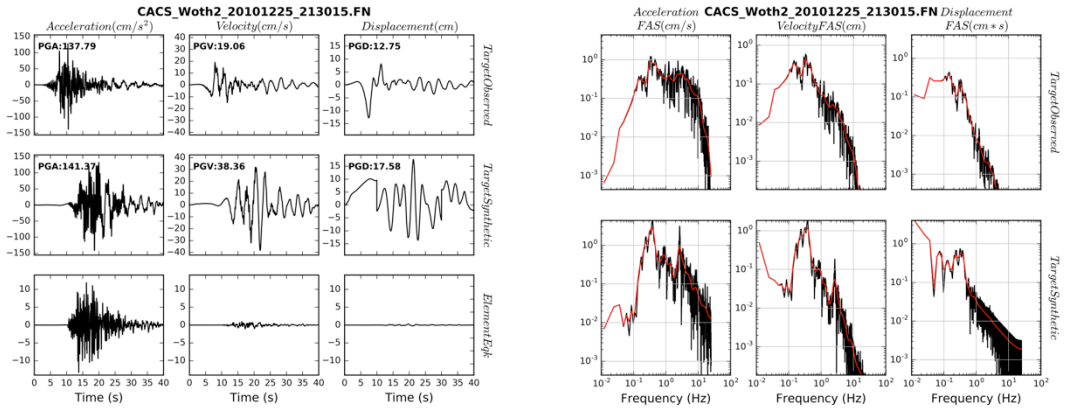


**Figure 32.** Comparison of simulations with data in the time and frequency domains for the fault-normal component, using as element event the 2010-12-25, 21:30:15, **M**4.7 earthquake for the Woth2 velocity profile.

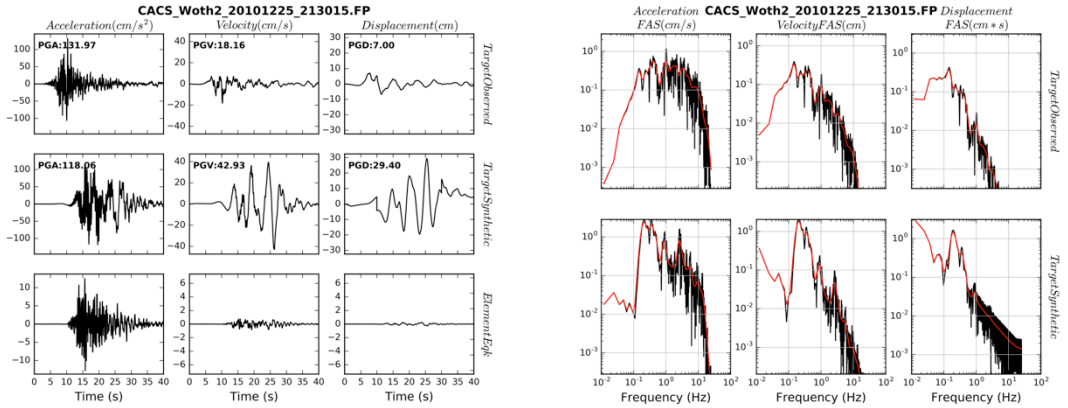


**Figure 33.** Comparison of simulations with data in the time and frequency domains for the fault-parallel component, using as element event the 2010-12-25, 21:30:15, **M**4.7 earthquake for the Woth2 velocity profile.

## Simulation of 2011-06-13, 02:20:49, M6.0 Event at CACS – Deconvolved

The values of the parameters used in the simulation of the 2011-06-13, 02:20:49, **M**6.0 Event at CACS are shown in Table 7. The comparison of the EGF results with the observed ground motions, using the 2010-12-25, 21:30:15, **M**4.7 as element event is shown in Figures 34 and 35 for the Woth1 $V_s$ profile and in Figures 36 and 37 for the Woth2 $V_s$ profile.

**Table 7.** Parameter values used in the EGF method.

| | **2010-10-25 21:30:15** | |
|---|---|---|
| Parameter | ***FN-component*** | ***FP-component*** |
| dx | 2.2 | 2.2 |
| dw | 1.8 | 1.8 |
| tra | 0.08 | 0.08 |
| nx | 5 | 5 |
| nw | 5 | 5 |
| nt | 5 | 5 |
| ntt | 28 | 28 |
| nsx | 5 | 5 |
| nsw | 5 | 5 |
| cfactor | 1.2 | 1.2 |
| ird | 2 | 2 |
| ipfm | 0 | 0 |
| Cmp | 90 | 0.0 |
| imdl | 3 | 3 |

## *2010-12-25, 21:30:15, M4.7 element event*

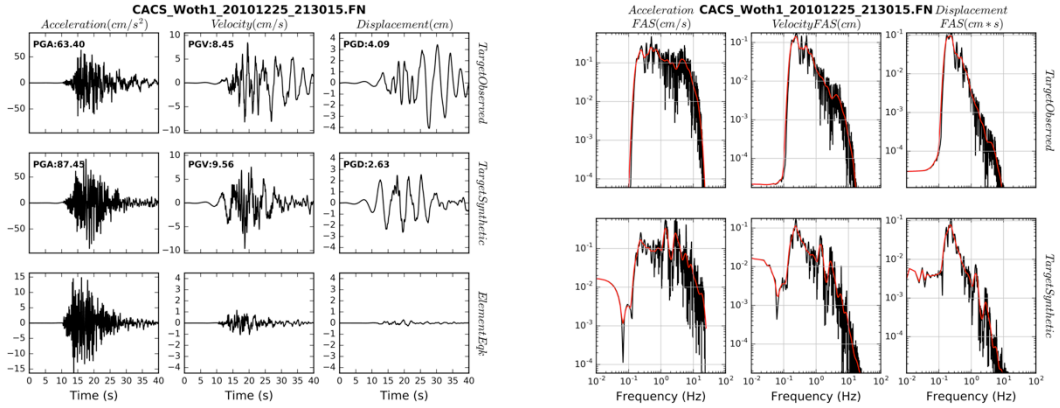


**Figure 34.** Comparison of simulations with data in the time and frequency domains for the fault-normal component, using as element event the 2010-12-25, 21:30:15, **M**4.7 earthquake for the Woth1 velocity profile.

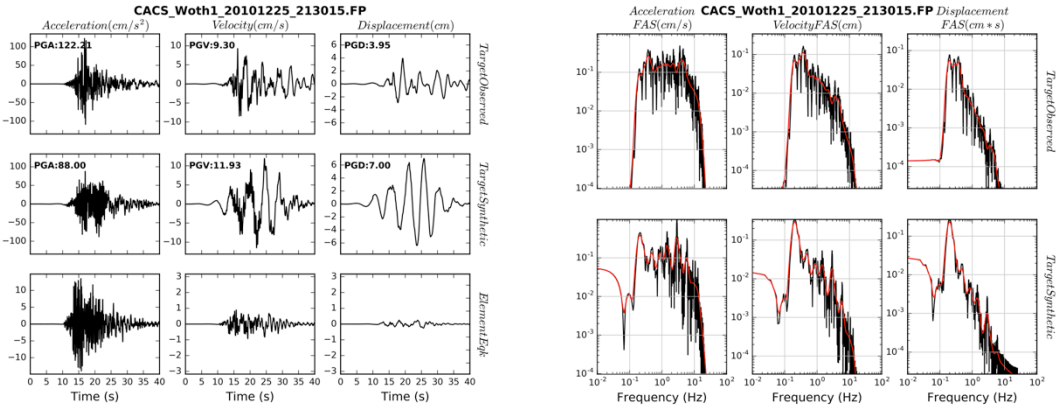


**Figure 35.** Comparison of simulations with data in the time and frequency domains for the fault-parallel component, using as element event the 2010-12-25, 21:30:15, **M**4.7 earthquake for the Woth1 velocity profile.

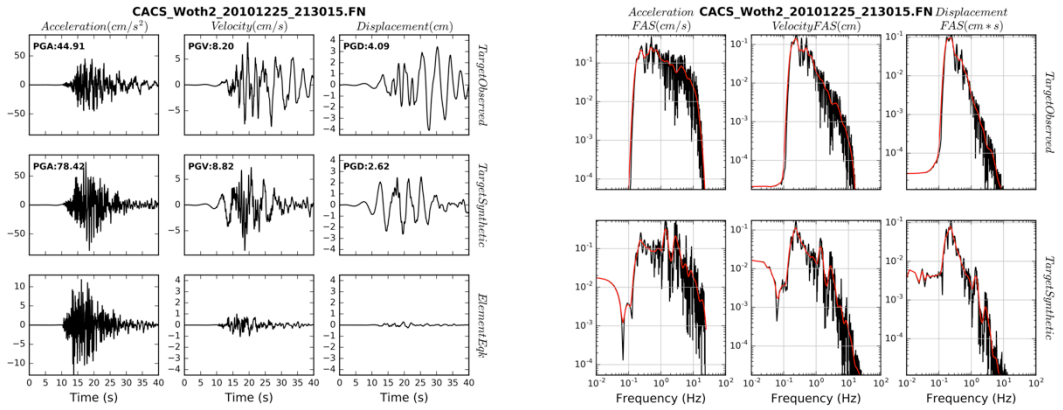


**Figure 36.** Comparison of simulations with data in the time and frequency domains for the fault-normal component, using as element event the 2010-12-25, 21:30:15, **M**4.7 earthquake for the Woth2 velocity profile.

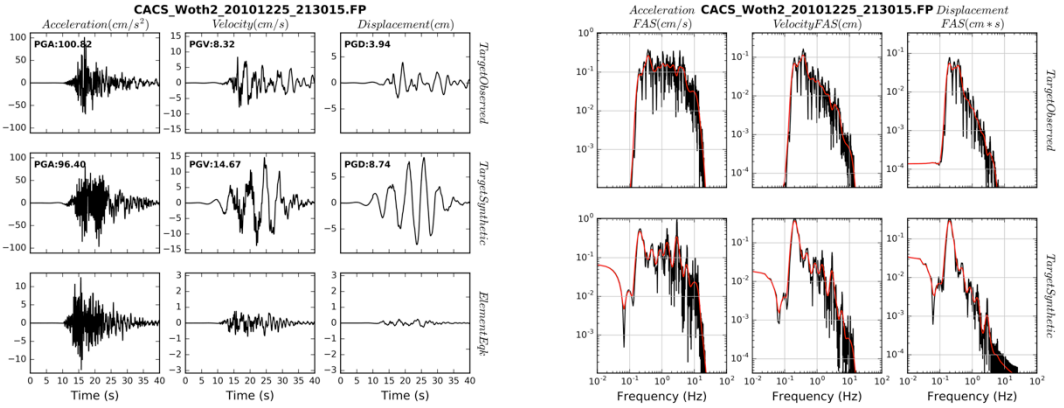


**Figure 37.** Comparison of simulations with data in the time and frequency domains for the fault-parallel component, using as element event the 2010-12-25, 21:30:15, **M**4.7 earthquake for the Woth2 velocity profile.

# Validation of the results

In the previous sections we presented comparisons between simulated and observed strong-motion waveforms in both time and frequency domain (FAS) for the selected events. These comparisons were mainly qualitative, and to quantify them we validated the simulations from the EGF approach using the Anderson (2004) Goodness-of-Fit (GoF) criteria. These GoF criteria examine a suite of different metrics and estimate a score for each one of these for different frequency bands.

Specifically, the waveforms are filtered into the ten pass-bands shown in Table 8 and a score is estimated for each one of these. Each frequency band is scored on ten different

criteria, in both the time and frequency domains, that are listed in Table 9. Each criterion is compared on a scale from 0 to 10, with 10 giving perfect agreement. The scoring function used for criteria C1-C9 is:

$$S(p_1, p_2) = 10exp\left\{-\left[\frac{(p_1 - p_2)}{\min(p_1, p_2)}\right]^2\right\} \quad (2)$$

where $p_1$ and $p_2$ are the specific criterion values for the observed and for the simulated waveforms. Criterion C10 is based on waveform cross-correlation and it does not use equation (2) for scoring.

**Table 8.** Frequency bands for applying the Anderson Goodness of Fit criteria.

| Band | Lower Frequency Limit (Hz) | Upper Frequency Limit (Hz) |
|---|---|---|
| B1 | 0.05 | 0.1 |
| B2 | 0.1 | 0.2 |
| B3 | 0.2 | 0.5 |
| B4 | 0.5 | 1.0 |
| B5 | 1.0 | 2.0 |
| B6 | 2.0 | 5.0 |
| B7 | 5.0 | 10.0 |
| B8 | 10.0 | 20.0 |
| B9 | 20.0 | 50.0 |
| B10 | 0.05 | 50.0 |

**Table 9.** List of the Anderson criteria for which we estimate the fit scores.

| Criterion | Name |
|---|---|
| C1 | Arias Duration |
| C2 | Energy Duration |
| C3 | Arias Intensity |
| C4 | Energy Integral |
| C5 | Peak Acceleration |
| C6 | Peak Velocity |
| C7 | Peak Displacement |
| C8 | Response Spectra |
| C9 | Fourier Spectra |
| C10 | Cross Correlation |

The overall quality of the fit for each record is estimated by averaging all the scores of all criteria over all frequency bands studied. The scores for all frequency bands for the 5 simulation sets previously described (3 for the LPCC and 2 for CACS sites) are shown in Figures 38-42.

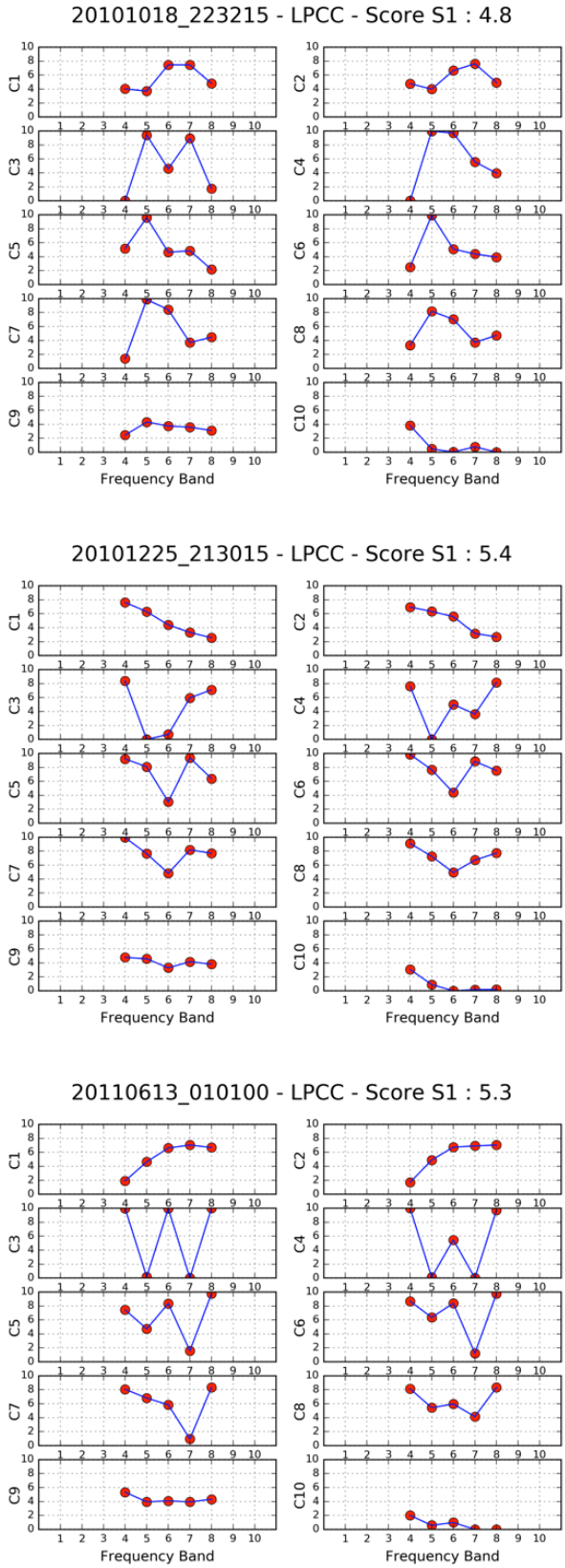


**Figure 38.** Plots of the Anderson GoF criteria scores for event 2011-02-21, 23:51:42 at LPCC site. Each plot corresponds to the results produced using a different element event.

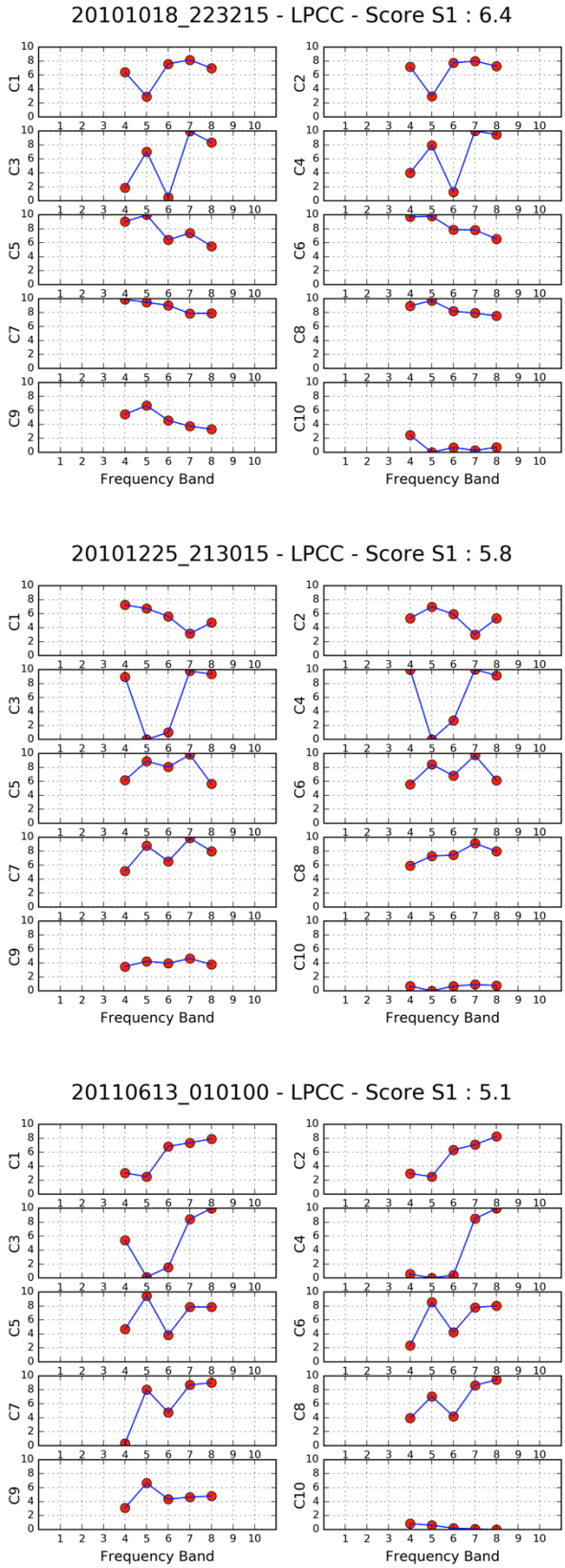


**Figure 39.** Plots of the Anderson GoF criteria scores for event 2011-06-13, 02:20:49 at LPCC site. Each plot corresponds to the results produced using a different element event.

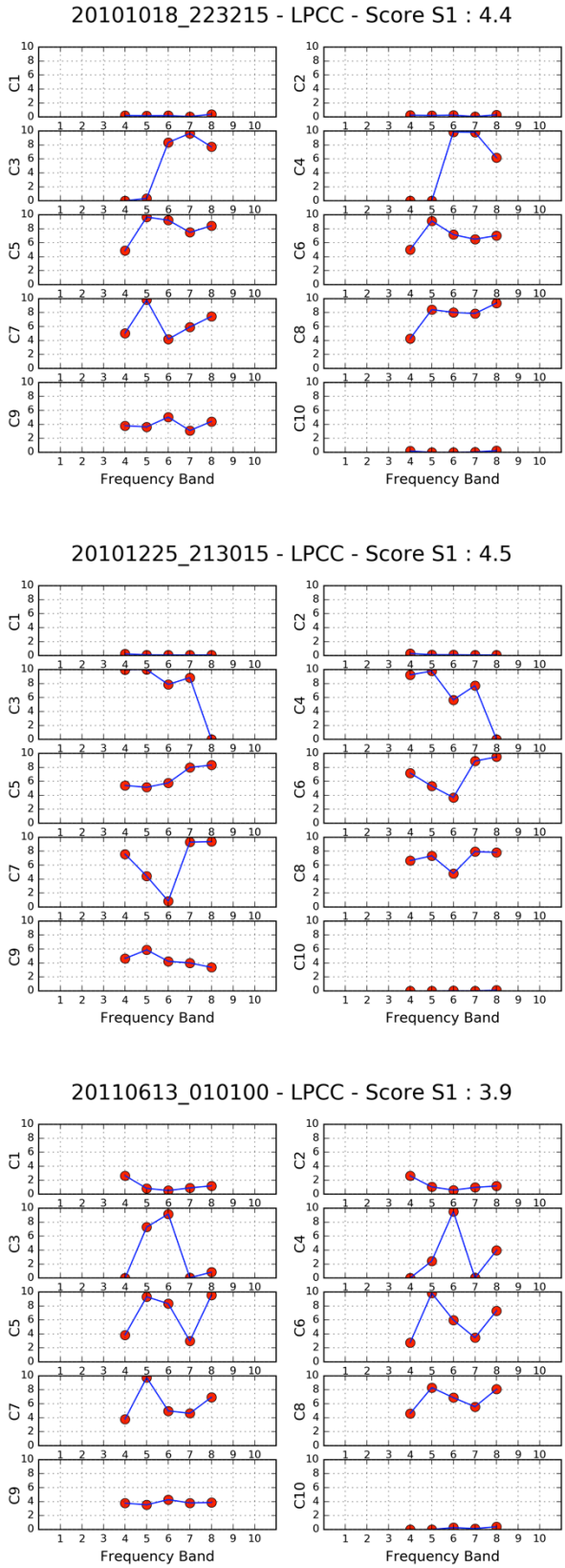


**Figure 40.** Plots of the Anderson GoF criteria scores for event 2011-12-23, 02:18:03 at LPCC site. Each plot corresponds to the results produced using a different element event.

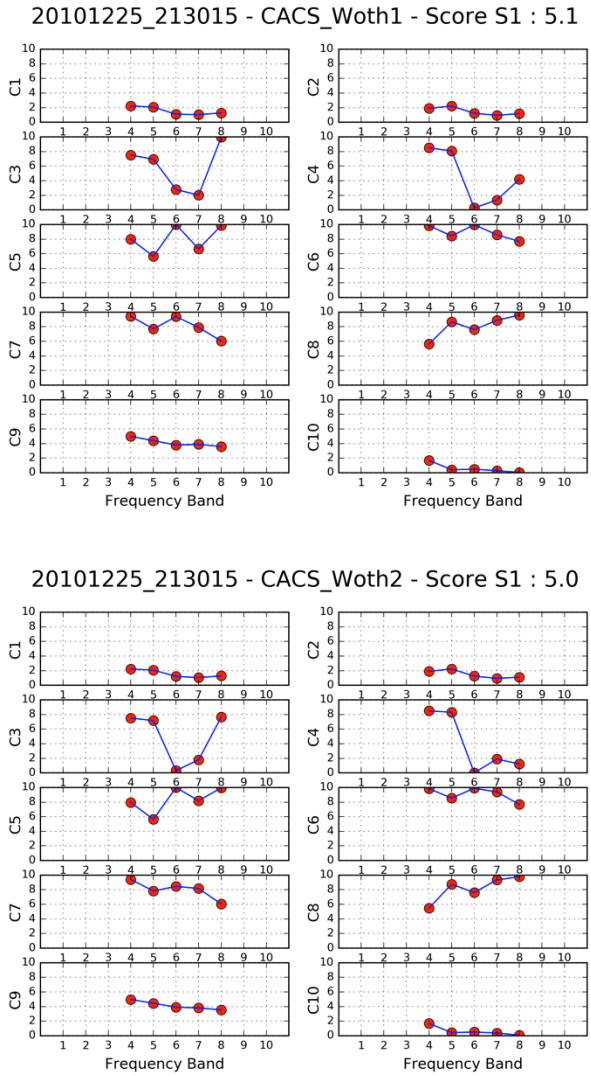


**Figure 41.** Plots of the Anderson GoF criteria scores for event 2011-02-21, 23:51:42 at CACS site, for the two $V_s$ profiles.

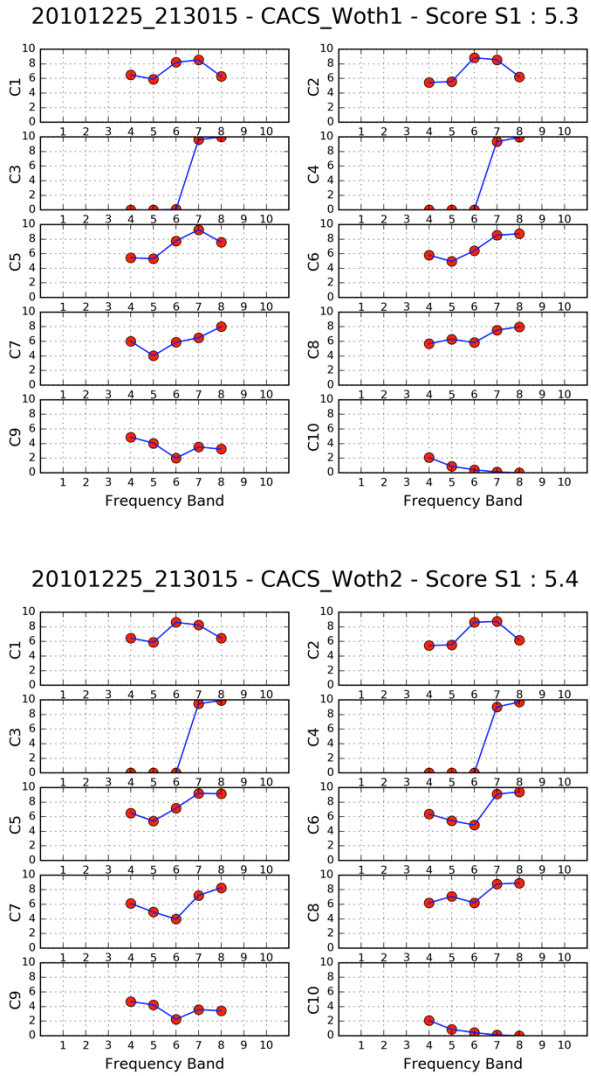


**Figure 42.** Plots of the Anderson GoF criteria scores for event 2011-06-13, 02:20:49 at CACS site, for the two $V_s$ profiles.

### *Performance against other simulation methods.*

Razafindrakoto et al. (2016; Rea16) performed hybrid ground motion simulations, using the Graves and Pitarka (2010) method, for the 2010-2011 Canterbury earthquake sequence. The simulations were performed using both 1D and 3D crustal structure models to examine the role of 3D basin conditions. In order to assess the performance of the EGF method we compare the Anderson overall fit of scores of the Rea16 simulations with those obtained using the EGF method. We use the Rea16 3D simulated waveforms at LPCC and CACS sites for the 2011-02-21, 23:51:42, **M**6.2 event, shown in Figures 41 and 42. The comparison shows good agreement with our results, exhibiting scores up to 5.1 for the CACS site. In the following we show the 3D Rea16 simulations together with the calculated Anderson GoF plots.

**Simulation of 2011-02-21, 23:51:42, M6.2 Event at LPCC**

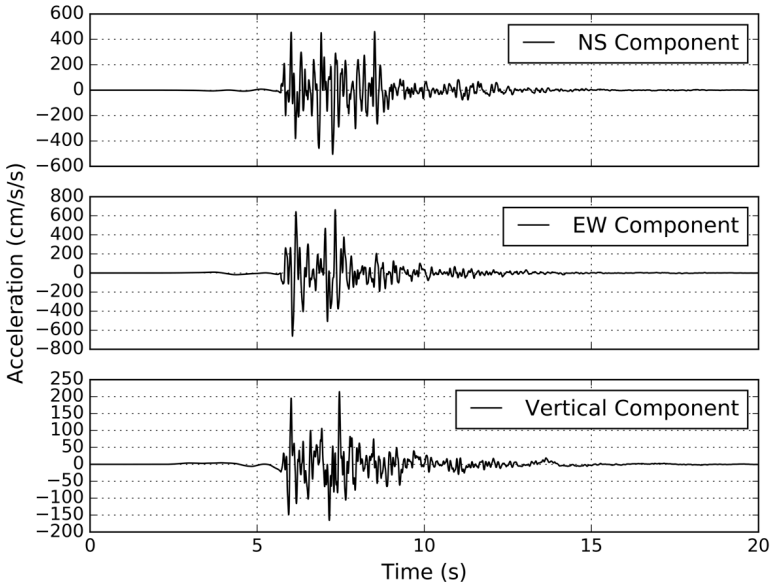


**Figure 41.** Synthetic time series at LPCC site for event 2011-02-21, 23:51:42.

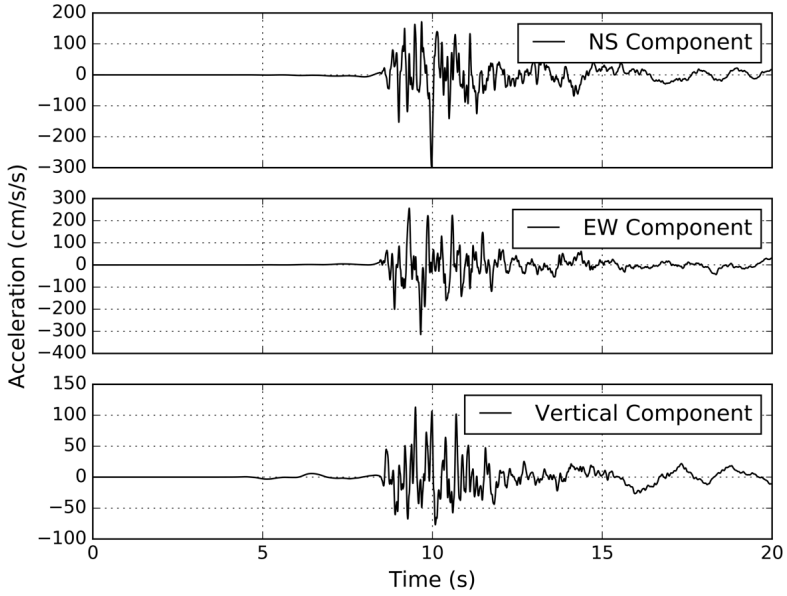


**Figure 42.** Synthetic time series at CACS site for event 2011-02-21, 23:51:42.

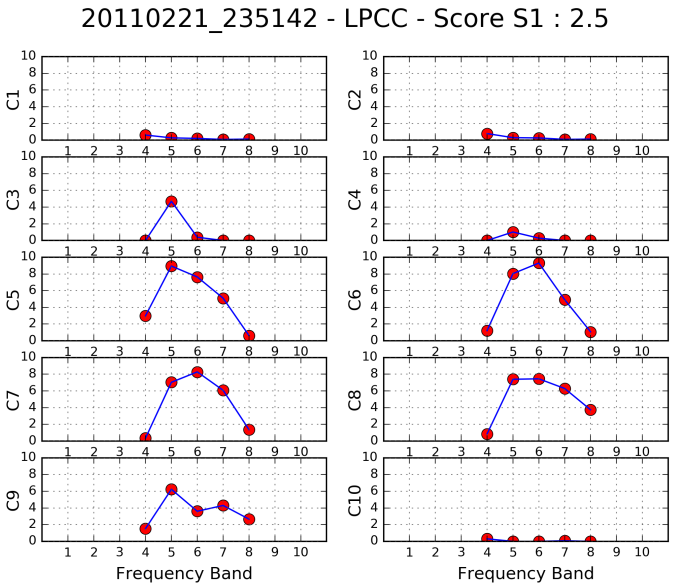


**Figure 43.** Plots of the Anderson GoF criteria scores for event 2011-02-21, 23:51:42at LPCC site.

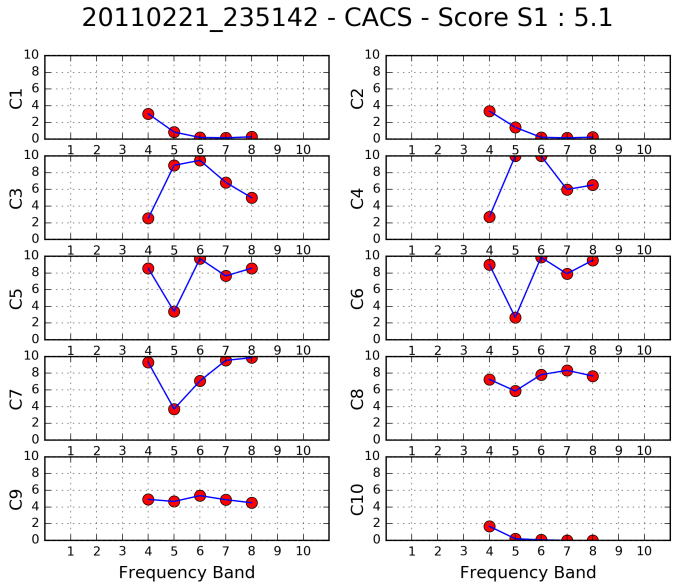


**Figure 44.** Plots of the Anderson GoF criteria scores for event 2011-02-21, 23:51:42 at CACS site.

# Summary and Conclusions

We used recordings of aftershocks of the Canterbury earthquake sequence and the empirical Green's functions method (EGF) to simulate the recorded ground motions of some of the largest events in this earthquake sequence, namely the 2011-02-21, 23:51:42, **M**6.2; 2011-06-13, 02:20:49, **M**6.0; and 2011-12-23, 02:18:03, **M**5.9 events.

There are several advantages to using the EGF approach in Christchurch. First, it does not require knowledge of the 3D structure or the calculation of Green's functions for that structure. Second, abundant strong motion recordings of aftershocks of the Canterbury earthquake sequence are available for this purpose. Third, the EGF method can be applied for modeling directivity and basin effects, both of which have been shown to be important for the Christchurch earthquake sequence.

In its standard form, the EGF method is not directly applicable to the modeling of nonlinear soil effects because it is based on the linear superposition of the EGFs. At short periods, standard EGF simulations will not account for the reduction of ground motion amplitudes due to nonlinear soil behavior. In order to account for the nonlinear soil behavior, we used as EGFs ground motion recordings deconvolved to a reference stiff soil condition representing the gravels that underlie the alluvial deposits.

We estimated the source models of the three selected events by using records of subenvents as empirical Green's functions having focal mechanisms and hypocentral distances similar to those of the three events we studied. We tested three subenvents in order to assess the sensitivity of the method to the different EGF's. We computed simulated waveforms for the Lyttelton Port strong motion station (LPCC), which we considered as a bedrock site in the absence of any other strong motion stations on the outcropping bedrock. We computed simulated waveforms for the Canterbury Aero Club site (CACS) using the deconvolved ground motions from two different soil profiles (two depths for the Riccarton gravel depth) to account for the epistemic uncertainty in the site characterization of this station.

We validated the simulations generated by the EGF approach using the Anderson (2004) Goodness-of-Fit (GoF) criteria. These GoF criteria examine a suite of different metrics and estimate a score for each one of these for different frequency bands. Further, in order to assess the performance of the EGF method, we compared the Anderson GoF scores of 3D broadband simulations performed by Razafindrakoto et al. (2016; Rea16) with those from this study. The overall scores are summarized in Table 10.

Based on the reported scores, the EGF method performs better for the February and June events, and worse for the December event. The 2011-06-13, 01:01:00 sub-event gave results with lower scores than the other two sub-events tested. This is the event with the largest magnitude of all three sub-events studied, so the worse performance could be partly attributed to the ratio of the main event/subevent magnitudes. The other two main

events have similar magnitudes and therefore their performance is mostly controlled by other parameters such as the source - site geometry and the degree of similarity between the focal mechanisms of the element and target events.

**Table 10.** Summary table of the overall quality of the fit as derived by averaging the individual Anderson GoF scores for the various element/target event combinations and for the broadband simulations of Razafindrakoto et al. (2016). The two values listed for CACS correspond to the results from the two alternative soil profiles for the site.

| ELEMENT EVENT /TARGET EVENT | 2011-02-21, 23:51:42 | | 2011-06-13, 02:20:49 | | 2011-12-23, 02:18:03 | |
|---|---|---|---|---|---|---|
| | LPCC | CACS | LPCC | CACS | LPCC | CACS |
| *2010-10-18, 22:32:15* | 4.8 | - | 6.4 | - | 4.4 | - |
| *2010-12-25, 21:30:15* | 5.4 | 5.1/5.0 | 5.8 | 5.3/5.4 | 4.5 | - |
| *2011-06-13, 01:01:00* | 5.3 | - | 5.1 | - | 3.9 | - |
| *Rea2016* | *2.5* | *5.1* | - | - | - | - |

Given the way that scores are calculated in the Anderson GoF, any score of about 6 and higher typically describes very good agreement between data and simulations. That is the case for the June event, for which the EGF method performs best among the three events studied.

The results from the deconvolved ground motions at both LPCC and CACS exhibit high overall scores. We were not able to see any significant differences between the results for the two soil profiles defined for the CACS site.

To obtain an independent measure of the performance of the EGF method, we used for comparison the results of the simulations for the February event from the Razafindrakoto et al. (2016) work. As can be seen in Table 10, the score for the CACS site is comparable with that obtained using the EGF method. However for LPCC, the score is significantly lower, which may result from the local site conditions not being fully represented by the available structure model.

Overall, the application of the EGF method to the Canterbury earthquake sequence showed the potential and the drawbacks of the method. One of the most important advantages is the simplicity of the method. By setting up very few parameters and by properly selecting the element event, we were able to produce high quality simulated waveforms. One of the most significant limitations of the method is that it cannot model the non-linear soil behavior which occurs under strong shaking due to the linear summation of the ground motions from each subevent. A second limitation of the method is that it typically cannot produce broadband simulated records. The frequency content of

the simulations is prescribed by the frequency content of the element event used, which is typically limited by background noise and/or instrument response. A useful extension of this work would be the application of the method to the Darfield earthquake and the testing of the method's capabilities in a more complex event.

## Acknowledgments

We would like to thank Prof. Brendon Bradley for sharing the results from the Finite-Difference simulations of Razafindrakoto et al. (2016). We would also like to thank Dr Christopher Markham and Prof. Jonathan Bray for providing us with the deconvolved ground motions at CACS and REHS sites in Christchurch.

## References

Anderson J.G., (2004). Quantitative Measure Of The Goodness-Of-Fit Of Synthetic Seismograms, *13th World Conference on Earthquake Engineering*, Vancouver, B.C., Canada, August 1-6, 2004 Paper No. 243.

Beavan J, Fielding E, Motagh M, Samsonov S and Donnelly N. (2011). Fault Location and Slip Distribution of the 22 February 2011 Mw 6.2 Christchurch, New Zealand, Earthquake from Geodetic Data. *Seism. Res. Lett.* 82, 789-799.

Beavan J., M. Motagh, E. J. Fielding, N. Donnelly & D. Collett, (2012). Fault slip models of the 2010–2011 Canterbury, New Zealand, earthquakes from geodetic data and observations of postseismic ground deformation, *New Zealand Journal of Geology and Geophysics* 55, 207-221.

Bradley, B.A., M. C. Quigley, R. Van Dissen, N. J. Litchfield, and W. Fry (2012). Ground Motion and Seismic Source Aspects of the Canterbury Earthquake Sequence, *in Proceedings of the 2012 NZSEE Conference*.

Bradley, B. A., Cubrinovski, M., 2011. Near-source strong ground motions observed in the 22 February 2011 Christchurch earthquake, *Bulletin of the New Zealand Society for Earthquake Engineering* 44, 181-194.

Brown, L.J. and Weeber, J.H. (1992) Geology of the Christchurch urban area, Institute of Geological and Nuclear Sciences, Lower Hutt.

Graves, R.W., and A. Pitarka (2010). Broadband Ground-Motion Simulation Using a Hybrid Approach, *Bull. Seismol. Soc. Am.* 100, 2095–2123.

Hartzell S., (1978). Earthquake aftershocks as Green's functions, *Geophys. Res. Lett.* 5, 1-4.

Holden, C. and J. Beavan (2012). Kinematic source studies of the ongoing 2010-2011) sequence of recent large earthquakes in Canterbury, *in Proceedings of the 2012 NZSEE Conference*.

Irikura, K. (1986). Prediction of strong acceleration motions using empirical Green's function, *in Proceedings 7th Japan Earthquake Engineering*, 151-156.

Irikura, K. and Kamae, K. 1994. Estimation of Strong Ground Motions in Broad-Frequency Band Based on Seismic Source Scaling Model and Empirical Green's Functions Technique, *Annali di Geofisica* 37, 1721-1743.

Irikura K., T. Kagawa, and H. Sekiguchi 1997. Revision of the empirical Green's function method (in Japanese), *Seism. Soc. of Japan* 2.

Kamae, K. and K. Irikura 1998. Source model of the 1995 Hyogo-ken Nanbu earthquake and simulation of near-source ground motion, *Bull. Seism. Soc. Am.* 88, 400-412.

Kamae, K., P.-Y. Bard, and K. Irikura 1998. Prediction of strong ground motion at EURO-SEISTEST site using the empirical Green's function method, *Journal of Seismology* 2, 193-207.

Konno, K. and T. Ohmachi (1998). Ground-motion characteristics estimated from spectral ratio between horizontal and vertical components of microtremor, *Bull. Seism. Soc. Am.* 88, 228-241.

Lawton, D.C., M. B. Bertram, K. W. Hall, K. L. Bertram, and J. Pettinga (2012). Post-earthquake seismic reflection survey, Christchurch, New Zealand, *SEG Las Vegas 2012 Annual Meeting*, DOI http://dx.doi.org/10.1190/segam2012-1270.1.

Leonard, M. (2010). Earthquake fault scaling: Self-consistent relating of rupture length, width, average displacement, and moment release, *Bull. Seismol. Soc. Am.* 100, 1971–1988.

Markham C, J. Macedo, and J.D. Bray, (2014). Evaluating Fully Nonlinear Effective Stress Site Response Analyses using Records from the Canterbury Earthquake Sequence, *Final report U.S.G.S. Award Number: G13AP00029*, 161pp.

Miyake H., Y. Tanaka, M. Sakaue, K. Koketsu, and Y. Ishigaki (2006). Empirical Green's function simulation of broadband ground motions on Genkai Island during the 2005 West Off Fukuoka Prefecture earthquake, *Earth Planets Space* 58, 1637–1642.

NZS 1170.5, (2004). Structural design actions, Part 5: Earthquake actions - New Zealand, Standards New Zealand.

Ordonez, G. (2000) "SHAKE2000," commercial software for performing seismic site response analysis.

Quigley, M., van Dissen, R., Litchfield, N., Villamor, P., Duffy, B., Barrell, D., Furlong, K., Stahl, T., Bilderback, E., and Noble, D., (2012). Surface rupture during the 2010 MW 7.1 Darfield (Canterbury) earthquake: Implications for fault rupture dynamics and seismic-hazard analysis, *Geology* 55–58. doi: 10.1130/G32528.1.

Razafindrakoto H.N.T., B.A. Bradley, R.W. Graves, (2016). Broadband ground motion simulation of the 2010-2011 Canterbury earthquake sequence, in Proceedings of the 2016 NZSEE Conference.

Silva, W. J., (1988). "Soil response to earthquake ground motion", *EPRI Report NP-5747*, Electric Power Research Institute, Palo Alto, California.

Somerville, P.G., N. Collins, N. Abrahamson, R. Graves and C. Saikia (2001). Earthquake source scaling and ground motion attenuation relations for the central and eastern United States, *Final report U.S.G.S. Award Number:* 99HQGR0098.

Wood, C.M., B.R. Cox, L.M. Wotherspoon, and R. Green (2012). Dynamic Site Characterization of Christchurch Strong Motion Stations, *in Proceedings of the 2012 NZSEE Conference*.